Cylindrical-Lens Light Sheets Generated from Circularly and Rectangularly Apertured Gaussian and Top-Hat Beams: A Unified Paraxial Diffraction Theory

Stoyan Yordanov* and Dimiter Prodanov*

Institute of Information and Communication Technologies – Bulgarian Academy of Sciences, Sofia, Bulgaria
*Corresponding authors: yordanov.stoyan@gmail.com; dimiter.prodanov@iict.bas.bg

Last Updated: 2026.10.29, 13:57:13 (Europe/Sofia, UTC+02:00)

Abstract

Cylindrical lenses are widely used to generate static light sheets, yet practical estimates of sheet thickness and propagation length are commonly based either on ideal Gaussian-beam formulas or on a one-dimensional slit model. A finite circular beam and circular hard stop couple the focused and non-focused pupil coordinates through the circular boundary. We develop a unified scalar paraxial diffraction theory for circularly and rectangularly apertured Gaussian and top-hat fields focused by a thin cylindrical lens. The principal analytical contribution is a Cartesian aperture-slice decomposition (CASD) of the finite circular-pupil cylindrical-lens field. Analytical integration along the focused pupil coordinate reduces the two-dimensional Fresnel diffraction integral to one numerical quadrature at any observation point, while retaining the coupling between the focused and non-focused coordinates imposed by the circular boundary. This reduction is exact within the scalar paraxial model. CASD extends to other two-dimensional apertures with Gaussian or top-hat illumination and quadratic pupil phase. The same propagation model yields complete separable solutions for rectangular Gaussian and top-hat pupils. We derive nominal-focal-plane, axial-propagation-plane, and optical-axis forms, including an incomplete-gamma axial series and a polar Bessel–incomplete-gamma series for the full focal region. Cartesian hypergeometric and recurrence-based incomplete-gamma series provide complementary full-field representations, with the former also supplying analytical moment coefficients. The intensity field defines the principal peak position, nominal- and peak-plane transverse full widths at half maximum (FWHMs), connected axial intensity FWHM, local sheet thickness, and integrated illumination. A further contribution is a common explicit moment-based formula for the nominal transverse FWHM, with geometry-specific coefficients connecting top-hat, truncated-Gaussian and effectively untruncated-Gaussian illumination continuously. Maximum relative errors against complete-field numerical widths remain below 0.5% on the tested domains for both pupil geometries. Exact profile roots and strong-focus approximations provide complementary axial-width relations. The circular slice field agrees with independent polar quadrature to a representative relative complex-field error below 8.8×10^{-9}. The theory quantifies finite-Fresnel focal displacement and the transition from top-hat to effectively untruncated Gaussian illumination while retaining the physical aperture, beam radius, wavelength, and focal length. A low-numerical-aperture air–glass–sample example illustrates refractive focus displacement and the distinct transverse and axial scaling.

Keywords: light-sheet microscopy; cylindrical lens; Fresnel diffraction; truncated Gaussian beam; top-hat beam; circular aperture; point-spread function; full width at half maximum.

1 Introduction

Light-sheet fluorescence microscopy illuminates a restricted plane of a specimen and observes fluorescence along an approximately orthogonal detection axis. This separation of illumination and detection enables rapid optical sectioning with reduced out-of-plane excitation and photodamage [1–3]. A static light sheet is often generated by focusing a collimated beam with a cylindrical lens, whereas digitally scanned systems synthesize the sheet from a rapidly translated pencil beam. In both cases, illumination design requires quantitative relations among incident beam size, aperture, focal length, wavelength, sheet thickness, height, and useful propagation length.

For a weakly truncated Gaussian beam, the focused direction is usually described by the Gaussian waist and Rayleigh range [4, 5]. For a uniform one-dimensional pupil, cylindrical focusing gives a sinc-squared focal profile and a Fresnel-integral defocus response [6]. Neither model is generally identical to the experimental combination of a circular Gaussian or top-hat beam, a circular iris, and a cylindrical lens. A circular stop is nonseparable in Cartesian coordinates: its available width along the focused coordinate depends on the coordinate parallel to the cylinder axis. Consequently, the sheet thickness can vary along its height, and the finite-Fresnel focal region need not be described by a single Gaussian or slit coefficient.

The broader theory of focused fields is extensive. McCutchen related lines through a three-dimensional diffraction image to projections of a generalized pupil [7]. Sheppard reduced the field along individual lines through an isotropic point focus to one-dimensional Fourier transforms for several two-dimensional aperture shapes [8]. Li and Wolf described deformation and displacement of the three-dimensional focal region as Fresnel number decreases [9], and Sheppard subsequently examined finite-Fresnel imaging for hard circular pupils and Gaussian beams [10]. Circular Gaussian pupils, truncation, axial irradiance, and aberration have been treated by Mahajan [11, 12], Li and Yu [13], Urey [14], and more recent moment-expansion approaches [15]. General circular-pupil focal fields with defocus and astigmatism can also be represented through the extended Nijboer–Zernike (ENZ) framework [16], including vector high-aperture extensions [17]. At the paraxial pupil-phase level, a cylindrical lens is the superposition of rotationally symmetric defocus and primary astigmatism.

Here we develop a unified finite-pupil formulation of one-axis cylindrical focusing, starting from the physical Fresnel diffraction integral for circular and rectangular hard stops illuminated by Gaussian and top-hat fields. The principal analytical contribution is a Cartesian aperture-slice decomposition (CASD) that analytically eliminates the focused pupil coordinate x' while retaining arbitrary observation coordinates (x, y, z). For a circular stop, the resulting one-dimensional quadrature preserves the coupling imposed by the circular boundary. Complete rectangular-pupil solutions follow from the same starting field and provide exact separable benchmarks. Building on this formulation, we derive complementary analytical field series and moment-based width expressions that connect the diffraction field directly to light-sheet dimensions. In particular, the nominal transverse-FWHM approximation has a common algebraic form for both pupil geometries, with geometry-specific coefficients retaining the continuous dependence on Gaussian truncation.

The main contributions are:

1. **Exact finite-circular-pupil reduction.** CASD (Cartesian aperture-slice decomposition) evaluates the focused pupil coordinate analytically, reducing the circular-pupil Fresnel field to one numerical quadrature at any observation point while retaining Gaussian truncation and the coupling between pupil coordinates. The construction generalizes to any bounded two-dimensional pupil geometry whose slices are unions of transmitting intervals, including elliptical apertures and pupils with gaps, for Gaussian or top-hat illumination and a pupil phase at most quadratic in the pupil coordinates.
2. **Continuous-truncation width expressions.** A common moment framework yields explicit nominal transverse-FWHM approximations for rectangular and circular pupils across top-hat, intermediate and effectively untruncated-Gaussian regimes, together with strong-focus axial-width approximations and separately established accuracy and applicability domains.
3. **Complementary analytical field representations.** Nominal-focal-plane, axial-propagation-plane and optical-axis specializations lead to an axial incomplete-gamma series and three full-focal-region representations: the polar Bessel–incomplete-gamma (PBIG), Cartesian hypergeometric (CHS) and recurrence-based incomplete-gamma (RIG) series. Their numerical comparison establishes their useful evaluation regimes, and CHS also supplies analytical coefficients for the moment-based width approximations.
4. **Quadratic-phase optical extensions.** The analytical slice reduction accommodates rotated or crossed cylindrical lenses, combined cylindrical–spherical systems, toroidal powers, tilt and decentration through the corresponding quadratic and linear pupil-phase terms.
5. **A practical connection between field structure and light-sheet dimensions.** A common metric framework quantifies focal displacement, nominal- and peak-plane transverse widths, connected axial FWHM and integrated illumination. A hierarchy of limiting formulas, continuous-truncation moment expressions and complete-field calculations identifies the appropriate description and its tested accuracy.
6. **Complete rectangular-pupil benchmarks.** Rectangular Gaussian and top-hat fields throughout the three-dimensional paraxial focal region are expressed as products of two one-dimensional finite strip integrals, providing exact separable benchmarks for the circular-pupil formulation.
7. **Three-layer refractive extension.** A low-NA air–glass–sample formulation relates refractive indices and layer thicknesses to focal displacement and the transverse and axial FWHM scales.

2 Optical model, pupil families, and notation

2.1 Geometry, coordinates, and scalar propagation assumptions

Figure 1 defines the coordinate system. Pupil coordinates are (x', y'), observation-plane coordinates are (x, y), and $z > 0$ is the physical propagation coordinate measured from the lens plane. The lens focuses from x' to x; its cylinder axis and the nominal sheet height are parallel to y' and y. An axial-propagation plane contains the optical z axis: the xz plane has $y = 0$, and the yz plane has $x = 0$. We use a monochromatic complex field with time dependence $\mathrm{Re}\{U(\mathbf{r})e^{-\mathrm{i}\omega t}\}$, where the real part is the physical field and U is its complex phasor. In a homogeneous medium of refractive index n,

$$\lambda = \frac{\lambda_0}{n}, \qquad k = \frac{2\pi}{\lambda} = \frac{2\pi n}{\lambda_0}, \tag{1}$$

where λ_0 is the vacuum wavelength. For a point (x', y') on an ideal cylindrical lens, the geometrical path from the lens to its line focus differs from the axial path by

$$\Delta R(x') = \sqrt{f^2 + x'^2} - f = \frac{x'^2}{2f} + O\left(\frac{x'^4}{f^3}\right). \tag{2}$$

With the stated $e^{-\mathrm{i}\omega t}$ convention and forward propagation proportional to $e^{\mathrm{i}kR}$, the lens must supply the compensating phase $e^{-\mathrm{i}k\Delta R}$. Its paraxial thin-lens transmission is therefore

$$t_{\mathrm{cyl}}(x') = \exp\left[-\frac{\mathrm{i}kx'^2}{2f}\right]. \tag{3}$$

There is no y'^2 term because an ideal cylindrical lens has no focusing power along its cylinder axis.

The model describes scalar monochromatic propagation in a homogeneous medium through an ideal thin cylindrical lens with a prescribed quadratic phase. Its paraxial regime is assessed below. Vector cylindrical focusing, including longitudinal polarization components, is treated by Purnapatra and Mondal [18]. Gillen *et al.* consider strongly focused, truncated Gaussian beams in a different, point-focusing geometry [19].

The Fresnel approximation follows by expanding the propagation distance through quadratic order. The leading neglected phase for a maximum transverse source–observation separation $\rho_{\max}$ is approximately

$$\Delta\phi_4 \simeq \frac{k\rho_{\max}^4}{8z^3}. \tag{4}$$

For $\lambda_0 = 633\,\mathrm{nm}$, $a = 5\,\mathrm{mm}$, and $z = 400\,\mathrm{mm}$ in air, Eq. 4 gives $\Delta\phi_4 \simeq 0.012$ rad, so the paraxial approximation is well within the intended accuracy. The same estimate provides a direct consistency check for other dimensions. Figure 3 provides a quantitative focal-region comparison of the paraxial and nonparaxial scalar cylindrical-lens models through their peak-normalized axial intensity profiles.

2.2 Apertures and incident beam families

For a centered axis-aligned rectangular stop, define

$$P_{\mathrm{rect}}(x', y') = \mathrm{rect}\left(\frac{x'}{2a_x}\right)\mathrm{rect}\left(\frac{y'}{2a_y}\right), \tag{5}$$

where $\mathrm{rect}(u) = 1$ for $|u| \le 1/2$ and 0 for $|u| > 1/2$; its value at the measure-zero boundary does not change the field.

For a circular hard stop,

$$P_{\mathrm{circ}}(x', y') = \mathrm{circ}\left(\frac{\sqrt{x'^2 + y'^2}}{a}\right), \tag{6}$$

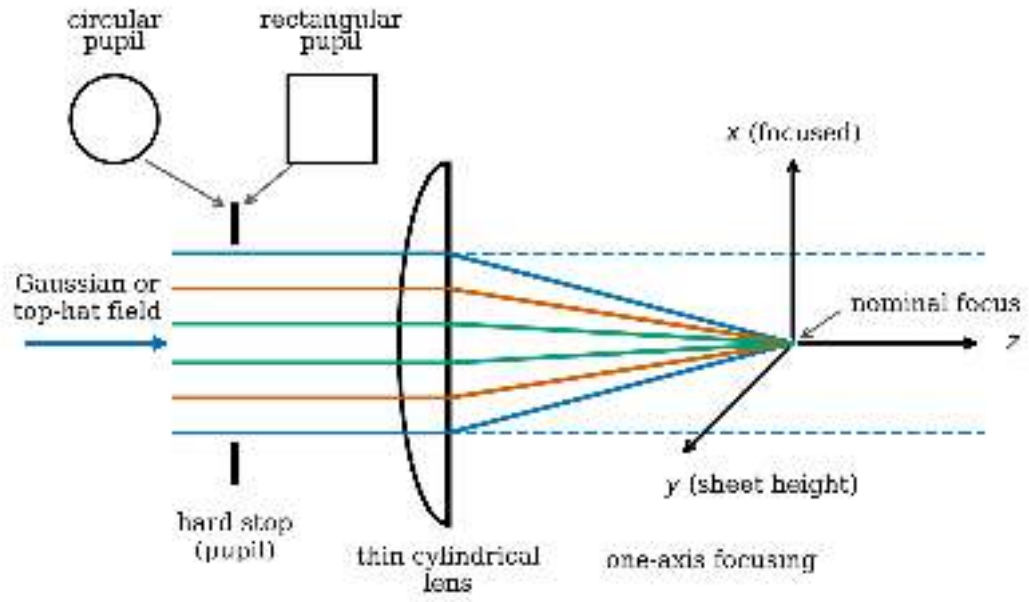


Figure 1: Physical geometry and coordinate convention. A circular or rectangular hard stop transmits a Gaussian or top-hat field, and a thin cylindrical lens focuses only the x direction. Parallel dashed blue guides schematically indicate the non-focused sheet-height extent.

$$P_{\mathrm{circ}}(x', y') = \begin{cases} 1, & x'^2 + y'^2 \le a^2, \\ 0, & x'^2 + y'^2 > a^2, \end{cases} \tag{7}$$

where $\mathrm{circ}(u) = 1$ for $0 \le u \le 1$ and 0 for $u > 1$. The circular pupil can be reconstructed as a continuous superposition of infinitesimally thin horizontal strips whose lengths vary with their height. At $|y'| < a$, the transmitting chord extends from $-L(y')$ to $L(y')$, with half-length $L(y') = \sqrt{a^2 - y'^2}$ and full length $2L(y')$. The pupil is zero for $|y'| > a$, while its interior has the equivalent representation

$$P_{\mathrm{circ}}(x', y') = \mathrm{rect}\left(\frac{y'}{2a}\right) \mathrm{rect}\left(\frac{x'}{2L(y')}\right). \tag{8}$$

The circular aperture can therefore be represented as two one-dimensional rectangle functions, but the focused-coordinate rectangle changes continuously with y' through $L(y')$. Each horizontal slice is the interval $-L(y') \le x' \le L(y')$. Section 3.2 develops this identity into Cartesian aperture-slice decomposition: the x' integral is evaluated analytically on every chord, leaving one exact integral over y'. Its circular-pupil specialization follows in Section 3.5.

Both pupil geometries are illuminated by the same Gaussian amplitude,

$$A_G(x', y') = A_0 \exp\left[-\frac{x'^2}{w_x^2} - \frac{y'^2}{w_y^2}\right]. \tag{9}$$

Here w_x, w_y are the field-amplitude $1/e$ radii, equivalently the intensity $1/e^2$ radii, at the lens. The rectangular family retains independent radii. The circular family below uses a round incident beam, $w_x = w_y = w_L$, so its amplitude is explicitly $A_G(x', y') = A_0 \exp\left[-\frac{x'^2 + y'^2}{w_L^2}\right]$. For either finite stop, top-hat illumination follows as $w_x, w_y \to \infty$, with $1/w_x^2$, $1/w_y^2 \to 0$ and $A_G \to A_0$ over the transmitting pupil; for the round beam this is the limit $w_L \to \infty$.

2.3 Illumination PSF and metric definitions

We define the global illumination point-spread function on a declared calculation domain by

$$\mathrm{PSF}_{\mathrm{ill}}(x,y,z) = \frac{|U(x,y,z)|^2}{\max_{x,y,z}|U(x,y,z)|^2}. \tag{10}$$

This illumination PSF describes the excitation field; an imaging-system PSF additionally includes the detection response. At fixed (y,z), the locally normalized focused-x-axis profile is

$$\mathrm{PSF}_x(x \mid y,z) = \frac{|U(x,y,z)|^2}{\max_x|U(x,y,z)|^2}. \tag{11}$$

Its connected principal-lobe FWHM is the local sheet thickness $\mathrm{FWHM}_x(y,z)$. Write $U_{\mathrm{ax}}(z) = U(0,0,z)$. For a smooth axial lobe, its intensity $I_{\mathrm{ax}} = |U_{\mathrm{ax}}|^2$ directly defines the focal peak. When resolved diffraction oscillations modulate a broader focal lobe, we also determine a broad profile I^B_{ax} by peak-protecting adaptive local quadratic regression. This profile follows the final broad focal peak while suppressing the faster oscillations; in smooth cases $I^B_{\mathrm{ax}} = I_{\mathrm{ax}}$. The cylindrical phase nominally focuses at f, whereas diffraction through a finite pupil can move this broad maximum to a different plane. The main scalar metrics are

$$\mathrm{FWHM}_{x,f} = \mathrm{FWHM}_x(0,f), \qquad \mathrm{FWHM}_{x,p} = \mathrm{FWHM}_x(0,z_p), \qquad z_p = \mathrm{peak}_{\mathcal{B}}\, I^B_{\mathrm{ax}}(z), \tag{12}$$

where $\mathcal{B}$ denotes the final resolved broad focal lobe. Its connected two-sided half-height width is FWHM_z. SI Section 2 specifies the peak selection, regression sensitivity, and independent half-height bracketing tests. The raw field remains the basis of every spatial intensity map and of the transverse width at the selected plane. A two-sided axial width is reported when both neighboring half-height crossings are resolved at positive z. If only the downstream crossing is established, its distance from the broad peak gives $\mathrm{HWHM}_{z,+}$; twice this distance is an equivalent axial extent for an asymmetric lobe, rather than a measured two-sided FWHM. The minimum-thickness plane z_t is searched only inside the established principal axial support. For the central section $y = 0$, write $\mathrm{FWHM}_x(z) = \mathrm{FWHM}_x(0,z)$, so that

$$\mathrm{FWHM}_{x,t} = \mathrm{FWHM}_x(z_t), \qquad \left.\frac{d\,\mathrm{FWHM}_x}{dz}\right|_{z_t} = 0, \qquad \left.\frac{d^2\mathrm{FWHM}_x}{dz^2}\right|_{z_t} > 0. \tag{13}$$

Nominal, peak-plane, and minimum thickness are thus evaluations of the same width function. The intensity peak and thickness minimum generally occur at different planes; all three evaluations coincide when $z_p = z_t = f$. The local peak and integrated illumination,

$$I_{\mathrm{peak}}(y,z) = \max_x |U(x,y,z)|^2, \qquad I_{\mathrm{int}}(y,z) = \int_{-\infty}^{\infty} |U(x,y,z)|^2 dx, \tag{14}$$

must accompany height-dependent width because a broad, weak lobe is not equivalent to a bright sheet.

The corresponding height and axial profiles are

$$\mathrm{PSF}_y(y \mid x,z) = \frac{|U(x,y,z)|^2}{\max_y|U(x,y,z)|^2}, \qquad \mathrm{PSF}_z(z \mid 0,0) = \frac{I^B_{\mathrm{ax}}(z)}{I^B_{\mathrm{ax}}(z_p)}, \tag{15}$$

with the latter restricted to the selected connected focal lobe. The ratio z_p/f records peak position, while $\mathrm{FWHM}_z = z_+ - z_-$ records the separation of its adjacent $\mathrm{PSF}_z = 1/2$ crossings. Axial FWHM is therefore peak-referenced by definition; the subscripts f and p distinguish the two transverse measurement planes. In the practical near-focus regime, $z_p \simeq f$ and the two transverse widths nearly coincide. The complete field retains the shifted-focus cases, whose branch selection and numerical closure are developed in the SI.

2.4 Dimensionless variables

For the circular pupil we define

$$\tilde{x} = \frac{ax}{\lambda f}, \qquad \tilde{y} = \frac{ay}{\lambda f}, \qquad \tilde{z} = \frac{z}{f}, \qquad \tau = \frac{a}{w_L}, \tag{16}$$

$$N_a = \frac{a^2}{\lambda f}, \qquad N_G = \frac{w_L^2}{\lambda f}, \qquad N_a = \tau^2 N_G. \tag{17}$$

The propagated circular field also depends on the local propagation number $N_z = a^2/(\lambda z) = N_a/\tilde{z}$. The three numbers have different roles: N_a couples the stop to the nominal focal distance, N_G couples the incident Gaussian radius to that distance, and N_z is the local phase-oscillation scale at the actual observation plane.

The axial definition $\tilde{z} = z/f$ identifies the nominal plane at $\tilde{z} = 1$ and is used in all dimensionless propagation maps. High-Fresnel panels resolve a smaller interval around 1 without changing coordinates. Transverse coordinates retain their diffraction scale. Dimensional companions in the SI state the physical radii, wavelength, and focal length; an equal-physical-scale view shows the long axial extent together with a separately labelled transverse magnification.

A compact reference to recurring symbols, their physical meanings and units is provided in SI Section 1.1.

2.5 Physical Regimes

The limiting path matters. At fixed a, f, and λ, letting $w_L \to \infty$ gives $\tau \to 0$, fixed N_a, and $N_G = N_a/\tau^2 \to \infty$: the field becomes top-hat over the fixed stop. An effectively untruncated Gaussian is obtained instead by expanding the stop size outward at fixed w_L and N_G, so $\tau \to \infty$ and $N_a = \tau^2 N_G \to \infty$. Increasing τ by shrinking w_L at fixed a is not the same physical limit.

Truncation determines how strongly the stop reshapes the incident Gaussian across its transmitting region. To orient the subsequent derivations, we first summarize the illumination regimes and practical width approximations developed in Section 3 and compared quantitatively in SI Section 12. Strong, intermediate and weak truncation distinguish the physical illumination profiles. The boundaries below provide a practical classification supported by the computed FWHM comparisons on the declared parameter domains:

$$\begin{aligned} 0 \le \tau \le 0.75 &: \quad \text{top-hat-like, strongly truncated Gaussian,} \\ 0.75 < \tau < 1.5 &: \quad \text{intermediate truncated Gaussian,} \\ \tau \ge 1.5 &: \quad \text{weakly truncated, approaching a Gaussian.} \end{aligned} \tag{18}$$

The choices $\tau = 0.75$ and 1.5 balance simple limiting formulas with a finite-truncation description where the profile changes appreciably. Their usefulness is quantified by the width errors summarized here and derived and assessed in the later sections. An accuracy requirement then selects the usable formula within each illumination region. Three complementary choices are developed below: a top-hat/finite-truncation/Gaussian three-formula rule; a simpler top-hat/Gaussian two-formula rule with a tested switching value; and moment formulas that retain τ continuously. The aperture-specific derivations appear in Sections 3.4 and 3.5. SI Section 12.1 compares their transverse and axial errors separately, gives the maximum in each named region, and locates the sampled 5%, 10%, 15%, 20%, and 25% thresholds. Peak-position accuracy is reported independently and does not set the FWHM boundaries.

The practical near-focus domain is defined by $|z_p/f - 1| \le 0.1$, with an extended comparison allowing 0.2. Width accuracy is assessed independently, so broad lobes remain included. On the sampled primary domain, the top-hat formulas over $0 \le \tau \le 0.75$ have maximum transverse errors of 9.70% and 7.78% for circular and square stops, respectively; their axial maxima are 20.16% and 45.14%. Over $1.5 \le \tau \le 3$, both Gaussian widths remain within 9.44%. In the intermediate region, the transverse moment formula stays within 0.313%, while the calibrated axial maxima are 20.85% and 19.90%. Thus a near-nominal peak alone does not guarantee an accurate axial asymptote. The SI supplies input-based sampled ranges that satisfy both the peak condition and a 10% or 15% axial-width target, permitting practical formula selection from (τ, N_a). A width-only two-formula switch at $\tau = 1.25$ gives a circular maximum of 25.00%; the square rule is less accurate because its top-hat endpoint already controls the maximum.

For a round Gaussian incident on a circular stop, the transmitted and excluded power fractions are $1 - e^{-2\tau^2}$ and $e^{-2\tau^2}$, respectively. At $\tau = 0.75$, the stop transmits 67.53% of the incident power; at $\tau = 1.5$ and 2 it

transmits 98.89% and 99.9665%. The corresponding excluded fractions, 32.47%, 1.11% and 0.0335%, support the progression from substantial truncation to effectively untruncated illumination. The width comparisons attach quantitative accuracy to these physical categories because coherent edge diffraction and the shape of the axial maximum also influence the focal metrics.

The truncation study in SI Section 12.4.1 and SI Figure 14 compares axial profiles and broad-peak positions for a finite circular stop and the corresponding untruncated Gaussian at the same incident beam radius and nominal focal length. It shows how the stop changes the focal profile, including cases with little excluded power; paired scalar-propagation checks assess the role of the paraxial approximation in those examples. Figure 3 addresses model accuracy over a wider dimensional parameter grid by comparing Fresnel propagation with quadratic cylindrical phase against Rayleigh–Sommerfeld-I (RS-I) propagation with the full cylindrical phase. RS-I supplies the nonparaxial scalar reference. Its simplified optical-distance kernel, denoted S-RS-I, retains the full source–observation distance and is checked against the full kernel, F-RS-I, as developed in SI Section 11.

Low ($N_a < 1$), transition ($1 \leq N_a < 10$), and high ($N_a \gg 1$) Fresnel numbers describe the strength of the pupil-phase variation and the approach to the central-chord limit. For a top-hat, high N_a suppresses nominal-to-peak displacement and gives the sinc-squared transverse limit. For a Gaussian, the corresponding focusing scale is also controlled by $N_G = N_a/\tau^2$: high N_a obtained solely by enlarging an already untruncated stop does not strengthen Gaussian focusing. Accordingly, neither $N_a = 10$ nor any other single aperture-number boundary guarantees $z_p \simeq f$ for arbitrary truncation. The field, peak, and width calculations retain both parameters.

The **strong-focus reduction** used for compact axial widths assumes a focal interval localized relative to f, over which the propagation prefactor and non-focused contribution vary slowly. It linearizes defocus about $z = f$; for a circular pupil it also uses the central-chord limit. Its quantitative scale and complete-field error are developed in Section 3.4. The practical near-focus criterion above tests peak position separately and retains wider lobes when their width errors are acceptable. Strong focus describes this axial localization, whereas paraxial validity concerns the propagation and lens-phase approximations.

The paraxial model approximates both propagation and cylindrical-lens phase. Equation 4 estimates the leading propagation residual as $k\rho_{\max}^4/(8z^3)$, where $\rho_{\max}$ is the largest transverse source–observation separation; at fixed separation it increases as z^{-3} toward the aperture. Propagation residuals below about 0.1 rad provide a useful small-phase screening criterion, while values approaching or exceeding 1 rad motivate direct field comparison. The full cylindrical phase also corrects the lens optical path, partly compensating the propagation residual near focus. At the axial nominal focus this compensation is exact on the focused meridian $y' = 0$, although the non-focused coordinate and geometrical amplitude still affect the field. Thus neither a/f alone nor a propagation-only phase threshold determines the combined model discrepancy. The SI gives the separate and combined residuals and quantitative examples.

Figure 3 compares the complete Fresnel field with quadratic cylindrical phase against S-RS-I propagation with the full cylindrical phase, for a circular top-hat and an untruncated round Gaussian. It covers $\lambda = 633$ nm, radii $a = 1$–100 mm for the top-hat or $w_L = 1$–100 mm for the Gaussian, and focal lengths $f = 10$–1000 mm. Here w_L is the $1/e$ amplitude radius; the Gaussian extends over the whole pupil plane without a hard stop. Each intensity is divided by its own refined principal peak. The relative RMS difference uses identical axial samples in the common focal window $z_p - 0.5f \leq z \leq z_p + 0.5f$, centered on the S-RS-I principal peak z_p, with focal-region resolution, equal sample weights and no alignment of peak positions. The paired maps therefore measure axial shape and focal-position differences around the reference focus between the paraxial and nonparaxial scalar cylindrical-lens models after removing overall peak-height differences. Equal numerical radii describe different radial amplitude distributions and do not imply equal incident power. SI Section 11 derives the full-phase reference, oscillation-aware integration, kernel checks and RMS definition, and distinguishes this focal-window comparison from the wider axial-domain score.

For example, at $f = 100$ mm the peak-normalized RMS differences are approximately 0.71% and 0.78% for $a = w_L = 10$ mm in the top-hat and Gaussian comparisons, respectively; at 50 mm they increase to 13.66% and 14.09%. These results illustrate why the coherent full-field comparison is more informative than a propagation-only edge-phase estimate near a compensated cylindrical focus.

The moment formulas provide a continuous description of truncation, from the top-hat limit through finite Gaussian illumination to the untruncated-Gaussian limit. The named illumination regions select convenient formulas; they do not restrict the continuous moment coefficients to the intermediate region. Their common dependence on amplitude moments avoids switching expressions at the named region boundaries. The transverse formula retains the circular pupil's non-focused Fresnel phase; the axial formulas use a strong-focus

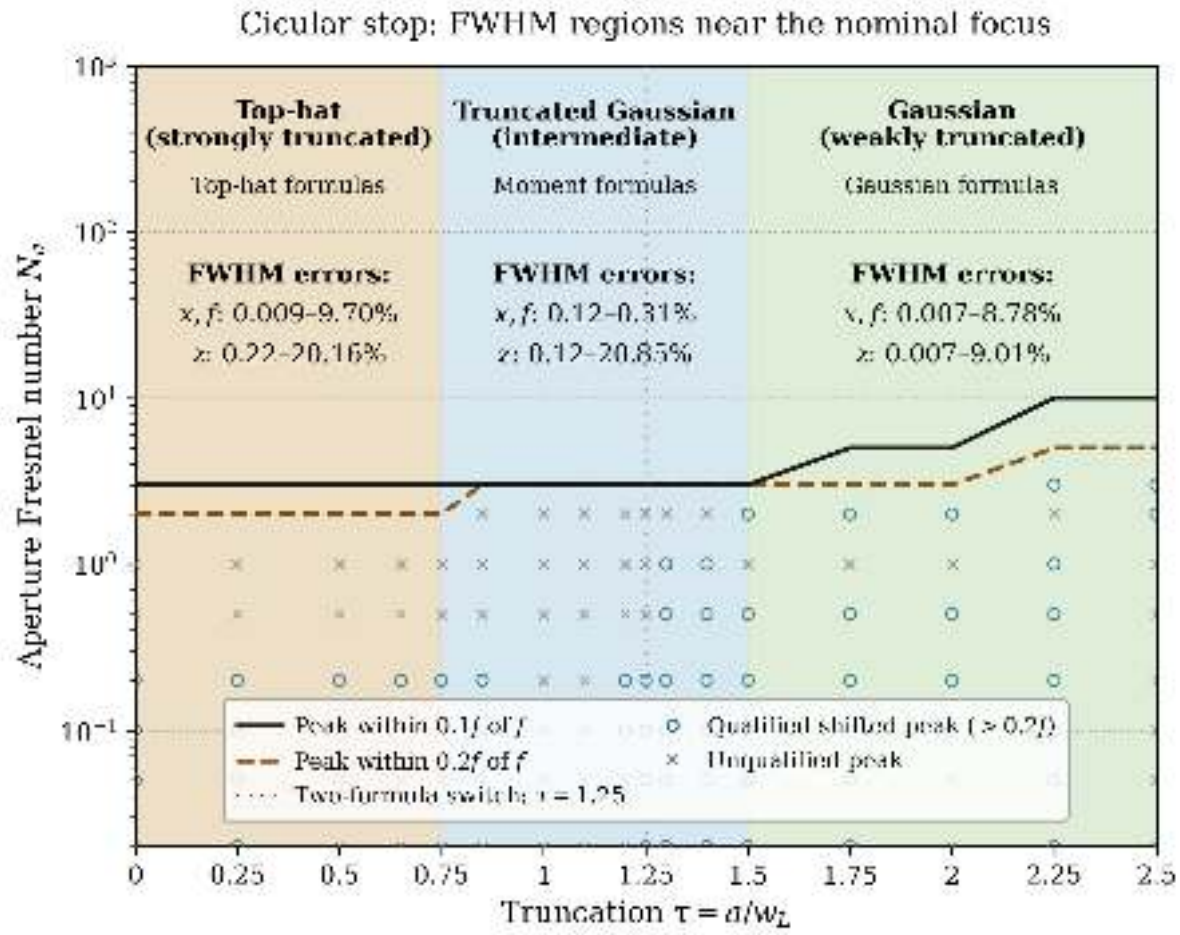


Figure 2: Circular-stop FWHM regions near nominal focus. The three-formula rule uses top-hat asymptotes for $0 \le \tau \le 0.75$, the derived transverse and calibrated axial moment formulas for $0.75 < \tau < 1.5$, and Gaussian formulas for $\tau \ge 1.5$. Labels give minimum–maximum sampled relative errors, $100|W_{\text{formula}}/W_{\text{reference}} - 1|$, for nominal transverse width $\text{FWHM}_{x,f}$ and broad-lobe axial width FWHM_z. References are qualified complete finite-pupil Fresnel widths with $|z_p/f - 1| \le 0.1$; accepted samples span $3 \le N_a \le 1000$, with qualification specific to each metric and parameter pair. The weak-region statistics include $1.5 \le \tau \le 3$, although the map ends at 2.5. Small minimum errors are sampled comparisons rather than numerical-accuracy guarantees. Solid and dashed curves summarize the sampled 10% and 20% peak-displacement criteria; open circles identify qualified peaks outside the extended 20% displacement criterion; gray crosses identify unqualified peaks. The vertical dotted line at $\tau = 1.25$ denotes the separate top-hat/Gaussian two-formula rule, whose maximum sampled width error is 25.00%. Dotted horizontal lines mark Fresnel decades.

strip reduction. For that strip profile, the derived axial expression has a maximum sampled root error of 12.60%, reduced to 0.768% by the endpoint-constrained calibration. Complete-field accuracy additionally depends on N_a and, in the Gaussian limit, N_G. The nominal transverse comparison in SI Figure 11 and the derived and calibrated axial comparisons in SI Figure 12 and SI Figure 13 cover $0.02 \le N_a \le 1000$ at $\tau = 0, 1, 1.5, 2, 3$, distinguish near-nominal from shifted peaks, and retain only qualified reference widths in the error curves. The nominal transverse formula remains within 0.497% on these 85 samples. The axial comparisons quantify the approach to practical explicit-formula accuracy and its deterioration outside strong focus, without imposing a single Fresnel-number cutoff for every truncation.

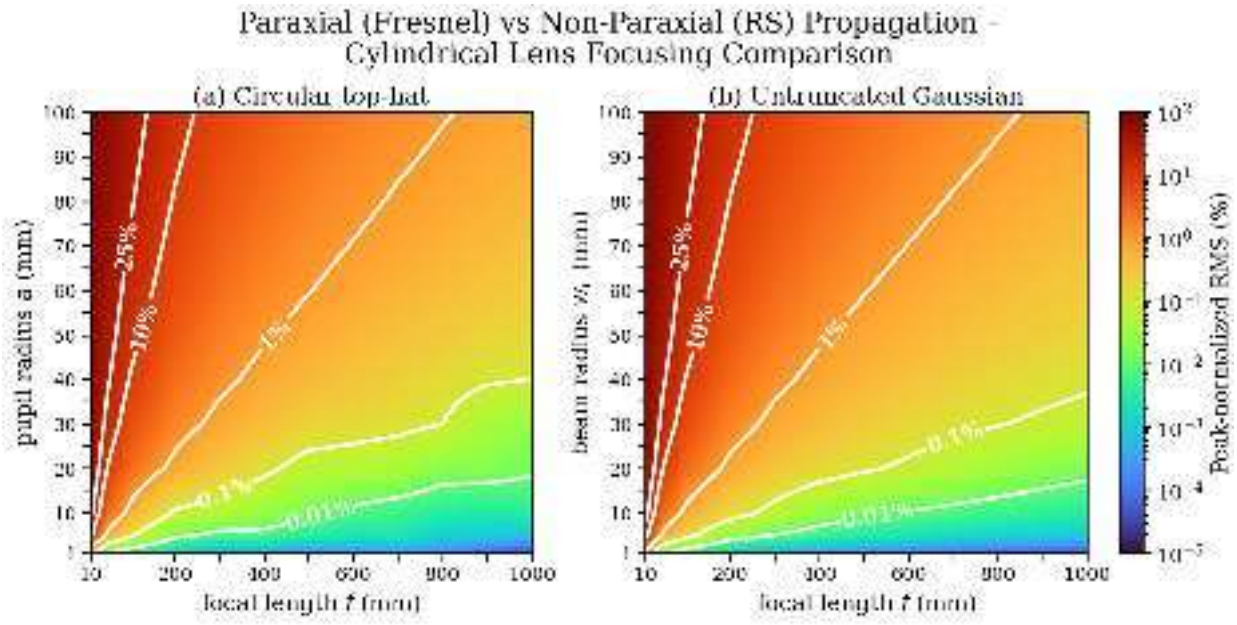


Figure 3: Peak-normalized axial RMS intensity difference between Fresnel propagation with quadratic cylindrical phase and S-RS-I propagation with full cylindrical phase at $\lambda = 633$ nm, in the common window $z_p - 0.5f \le z \le z_p + 0.5f$ centered on the S-RS-I principal peak: (a) circular top-hat with hard-stop radius a; (b) untruncated round Gaussian with $1/e$ amplitude radius w_L. Each intensity is divided by its independently refined principal peak, without aligning the peak positions. Focal length $f = 10$–1000 mm is horizontal and the respective radius, 1–100 mm, is vertical. Each Fresnel/RS pair uses identical retained axial samples; the two panels share a logarithmic percentage scale. White contours mark 0.01%, 0.1%, 1%, 10% and 25% where attained; colors and contours interpolate logarithms of qualified values on the 144-geometry grid per family. The incident amplitude is identical within each model pair; both the propagation and lens-phase approximation change in this scalar-model comparison. Off-axis points are excluded from the RMS.

3 Paraxial focal-field theory of a cylindrical lens

3.1 General three-dimensional Fresnel diffraction formulation

Let $A(x', y')$ contain the incident amplitude, $P(x', y')$ be the pupil (aperture) function, and $\Phi_{\text{add}}(x', y')$ denote any additional prescribed pupil phase. Immediately after the lens,

$$U_L(x', y') = A(x', y')P(x', y')e^{\mathrm{i}\Phi_{\text{add}}(x', y')}t_{\text{cyl}}(x'). \tag{19}$$

Fresnel propagation gives [20, 21]

$$U(x, y, z) = \frac{e^{\mathrm{i}kz}}{\mathrm{i}\lambda z} \iint U_L(x', y') \exp\left[\frac{\mathrm{i}k}{2z}((x - x')^2 + (y - y')^2)\right] dx'\, dy'. \tag{20}$$

After expanding the squares and substituting t_{cyl}, the geometry-independent field is

$$U(x,y,z) = C(x,y,z) \iint_{\mathcal{D}} A(x',y') e^{\mathrm{i}\Phi_{\mathrm{add}}(x',y')} \times \exp\left[\frac{\mathrm{i}k}{2}\left(\frac{1}{z}-\frac{1}{f}\right)x'^2 + \frac{\mathrm{i}k y'^2}{2z} - \mathrm{i}q_x x' - \mathrm{i}q_y y'\right] dx'\,dy', \tag{21}$$

where

$$C(x,y,z) = \frac{e^{\mathrm{i}kz}}{\mathrm{i}\lambda z}\exp\left[\frac{\mathrm{i}k(x^2+y^2)}{2z}\right], \qquad q_x = \frac{kx}{z}, \quad q_y = \frac{ky}{z}, \tag{22}$$

Here A specifies the incident field and Φ_{add} contains any phase beyond the ideal cylindrical lens. For the hard stops considered here, P is one inside the transmitting domain $\mathcal{D}$ and zero outside, so restricting the integral to $\mathcal{D}$ incorporates the pupil function. The rectangular domain is $\mathcal{D}_{\mathrm{rect}} = [-a_x, a_x]\times[-a_y, a_y]$, and the circular domain is $\mathcal{D}_{\mathrm{circ}} = \{(x',y') : x'^2 + y'^2 \le a^2\}$. Expansion separates the observation-only phase in C from the pupil variables; collecting the like quadratic and linear powers of x' and y' then exposes the coefficients common to both geometries. With the elliptical Gaussian amplitude $A(x',y') = A_0\exp[-x'^2/w_x^2 - y'^2/w_y^2]$, its two real quadratic terms combine with the propagation and lens phases to give

$$\beta_x = \frac{1}{w_x^2} - \frac{\mathrm{i}k}{2}\left(\frac{1}{z}-\frac{1}{f}\right), \qquad \beta_y = \frac{1}{w_y^2} - \frac{\mathrm{i}k}{2z}. \tag{23}$$

For $\Phi_{\mathrm{add}} = 0$, Eq. 21 becomes the common rectangular–circular Gaussian field

$$U_{\mathcal{D}}(x,y,z) = CA_0 \iint_{\mathcal{D}} \exp[-\beta_x x'^2 - \beta_y y'^2 - \mathrm{i}q_x x' - \mathrm{i}q_y y']dx'\,dy'. \tag{24}$$

The Gaussian amplitude is fully included in β_x and β_y. The pupil geometry enters through $\mathcal{D}$; the rectangular branch retains independent radii, while the circular illumination family below sets $w_x = w_y = w_L$. For either hard stop, uniform top-hat illumination follows continuously as

$$w_x, w_y \to \infty, \qquad \frac{1}{w_x^2}, \frac{1}{w_y^2} \to 0, \tag{25}$$

applied after the coefficients have been formed. The physical $1/z$ prefactor is retained because it affects axial intensity, peak position, and axial FWHM.

3.2 Common Cartesian aperture-slice formulation and strip integral

The rectangular and circular domains in Eq. 24 can be treated by integrating first along the focused pupil coordinate. At each fixed y', describe the transmitting chord by its half-width $L(y')$:

$$\mathcal{D} = \{(x',y') : y' \in \mathcal{Y},\ -L(y') \le x' \le L(y')\}. \tag{26}$$

For the two pupils studied here, and for an axis-aligned ellipse as a further example, the chord functions are

$$L(y') = \begin{cases} a_x, & |y'| \le a_y \quad \text{(rectangle)},\\ \sqrt{a^2 - y'^2}, & |y'| \le a \quad \text{(circle)},\\ a_x\sqrt{1-(y'/a_y)^2}, & |y'| \le a_y \quad \text{(ellipse)}. \end{cases} \tag{27}$$

Here $\mathcal{Y}$ is the corresponding range of y', and a_x, a_y denote the ellipse's semiaxes in the last line. A strip of infinitesimal height dy' and length $2L(y')$ contributes to a continuous superposition that reconstructs the aperture. More general bounded apertures are described by their transmitting cross-sections, which may contain one or several disjoint intervals. Integrating the complex contributions over these intervals and then over y' reconstructs the coherent field; the interval-sum form is given below. The ellipse illustrates the same

reduction for unequal transverse dimensions. We develop the field and FWHM specializations below for the rectangular and circular pupils.

The circular example is illustrated in Figure 4. Grouping the integrand of Eq. 24 by pupil coordinate makes the reduction explicit:

$$U_{\mathcal{D}}(x,y,z) = CA_0 \int_{y'\in\mathcal{Y}} e^{-\beta_y y'^2 - \mathrm{i}q_y y'} \left[\int_{x'\in\mathcal{D}_{y'}} e^{-\beta_x x'^2 - \mathrm{i}q_x x'} \, dx' \right] dy'. \tag{28}$$

Each coordinate has the same quadratic–linear exponential kernel. Its integral over a symmetric interval is the one-dimensional finite strip function

$$S(\beta, q; h) = \int_{-h}^{h} e^{-\beta u^2 - \mathrm{i}qu} du. \tag{29}$$

Completing the square is useful because it converts the quadratic–linear exponent into a standard finite Gaussian antiderivative:

$$-\beta u^2 - \mathrm{i}qu = -\beta \left(u + \frac{\mathrm{i}q}{2\beta} \right)^2 - \frac{q^2}{4\beta}, \tag{30}$$

Here the principal square root is the branch $\sqrt{\beta} = \sqrt{|\beta|} e^{\mathrm{i}\arg(\beta)/2}$ with $-\pi < \arg(\beta) \le \pi$. With this branch, the shifted endpoints are $\pm\sqrt{\beta}h + \mathrm{i}q/(2\sqrt{\beta})$. Evaluating the antiderivative at those endpoints and using the oddness of erf gives the symmetric sum

$$S(\beta, q; h) = \frac{\sqrt{\pi}}{2\sqrt{\beta}} e^{-q^2/(4\beta)} \left[\mathrm{erf}\left(\sqrt{\beta}h + \frac{\mathrm{i}q}{2\sqrt{\beta}} \right) + \mathrm{erf}\left(\sqrt{\beta}h - \frac{\mathrm{i}q}{2\sqrt{\beta}} \right) \right], \tag{31}$$

The finite strip integral remains regular at $\beta = 0$: on $[-h, h]$, $e^{-\beta u^2}$ tends uniformly to one, so the limit may be taken inside the integral. Evaluating the remaining exponential gives the continuous strip integral branch,

$$\begin{aligned} S(0, q; h) = \int_{-h}^{h} e^{-\mathrm{i}qu} du &= \begin{cases} 2\sin(qh)/q, & q \neq 0, \\ 2h, & q = 0, \end{cases} \\ &= 2h \, \mathrm{sinc}(qh), \qquad \mathrm{sinc}(u) = \frac{\sin(u)}{u}, \quad \mathrm{sinc}(0) = 1. \end{aligned} \tag{32}$$

This branch is the continuous value of the original integral where the separate factors of the error-function expression are singular. It is distinct from the choice of square-root branch used for $\beta \neq 0$. Substituting $h = L(y')$ into the strip evaluates the focused-coordinate integral analytically. The common field becomes

$$U_{\mathcal{D}}(x,y,z) = C(x,y,z)A_0 \int_{y} e^{-\beta_y y'^2 - \mathrm{i}q_y y'} S(\beta_x, q_x; L(y')) \, dy'. \tag{33}$$

This Cartesian aperture-slice decomposition is exact within the Fresnel model. In general the integration limits couple the coordinates even though the displayed exponential factors are separated. A rectangular stop has constant $L = a_x$, so its focused strip factors out of the remaining integral, which is itself a strip of half-width a_y. A circular stop retains the variable chord $\sqrt{a^2 - y'^2}$ and therefore one coupled quadrature. The same distinction will enter their moment coefficients and transverse widths. SI Section 3 develops the common endpoint construction, including the limiting branches and interval sums used below.

Slices containing gaps are treated by listing their disjoint transmitting intervals rather than using one outer half-width. If $\mathcal{D}_{y'}$ is such a slice, then

$$\mathcal{D}_{y'} = \bigcup_{m=1}^{n(y')} [\ell_m(y'), r_m(y')],$$
$$\int_{\mathcal{D}_{y'}} e^{-\beta_x x'^2 - \mathrm{i}q_x x'}\, dx' = \sum_{m=1}^{n(y')} \int_{\ell_m(y')}^{r_m(y')} e^{-\beta_x x'^2 - \mathrm{i}q_x x'}\, dx'. \tag{34}$$

Each interval uses the same error-function antiderivative evaluated at its two endpoints. Their complex amplitudes are summed before intensity is formed. This includes annular and polygonal pupils, including star-shaped stops; sharp boundaries change the interval endpoints, not the analytical inner integral. The outer quadrature can be split where the interval structure changes. SI Section 7 gives the endpoint formula and its continuous limits. For the centered rectangle and circle, Eq. 33 is the single-interval form used throughout the following derivations.

3.3 Moment expansion of the Fresnel field and FWHM approximations

The exact field supplies a transverse width through a half-height root. A complementary approach is the moment expansion of an integral: the integrand is separated into a weight and a factor whose dependence on the observation coordinate can be expanded. Here that factor is an exponential. For an integrable weight $W(s)$ on a bounded interval, the basic operation is

$$\begin{aligned} F(v) &= \int_{-h}^{h} g(v,s)\, ds = \int_{-h}^{h} W(s) e^{-\mathrm{i}vs} ds \\ &= \int_{-h}^{h} W(s) \left[\sum_{n=0}^{\infty} \frac{(-\mathrm{i}v)^n s^n}{n!} \right] ds \\ &= \sum_{n=0}^{\infty} \frac{(-\mathrm{i}v)^n}{n!} M_n. \end{aligned} \tag{35}$$

where the coefficients are the weighted moments

$$M_n = \int_{-h}^{h} s^n W(s)\, ds. \tag{36}$$

The exponential series converges uniformly on bounded sets of v and s, permitting integration term by term. Each coefficient is obtained by integrating one power of the pupil coordinate against the same weight. This replaces repeated field evaluations along a transverse profile by coefficient evaluation followed by a local half-height approximation. It also gives the rectangular and circular pupils the same transverse FWHM formula: their geometry enters through the reference size and the moments, rather than through a different width construction.

At $y = 0$ and a prescribed positive z, introduce

$$a_0 = \begin{cases} a_x, & \text{rectangle,} \\ a, & \text{circle,} \end{cases} \qquad s = \frac{x'}{a_0}, \quad t = \frac{y'}{a_0}, \quad v = \frac{k a_0 x}{z}. \tag{37}$$

The scaled domain $\widehat{\mathcal{D}}$ is the transmitting pupil in (s,t) coordinates: $|s| \le 1$, $|t| \le a_y/a_x$ for the rectangle, and $s^2 + t^2 \le 1$ for the circle. Collect the Gaussian amplitude and quadratic pupil phases in the weight

$$W_z(s,t) = e^{-a_0^2 \beta_x(z) s^2 - a_0^2 \beta_y(z) t^2}. \tag{38}$$

The exponent of W_z is quadratic in the pupil coordinates. Its complex coefficients retain both Gaussian attenuation and propagation phase. To obtain a normalized transverse field, divide by the on-axis value at the same positive z and remove the observation-only phase. Substituting the pupil integrals makes these operations explicit:

$$\begin{aligned}\phi(v;z) &= e^{-\mathrm{i}kx^2/(2z)}\frac{U_{\mathcal{D}}(x,0,z)}{U_{\mathcal{D}}(0,0,z)} \\ &= e^{-\mathrm{i}kx^2/(2z)}\frac{C(x,0,z)}{C(0,0,z)}\frac{\iint_{\mathcal{D}} e^{-\beta_x x'^2-\beta_y y'^2}e^{-\mathrm{i}kxx'/z}dx'\,dy'}{\iint_{\mathcal{D}} e^{-\beta_x x'^2-\beta_y y'^2}dx'\,dy'}.\end{aligned} \tag{39}$$

We introduce this compensating phase factor to cancel the observation-only phase in C and isolate the normalized pupil integral. Here A_0 cancels, and $C(x,0,z)/C(0,0,z) = e^{\mathrm{i}kx^2/(2z)}$ cancels the displayed observation phase. Scaling $x' = a_0 s$ and $y' = a_0 t$ also cancels the common Jacobian a_0^2. The resulting dimensionless field is

$$\phi(v;z) = \frac{\iint_{\widehat{\mathcal{D}}} W_z(s,t)e^{-\mathrm{i}vs}\,ds\,dt}{\iint_{\widehat{\mathcal{D}}} W_z(s,t)\,ds\,dt}. \tag{40}$$

This displays the same weight–exponential split as Eq. 35. The factor $e^{-\mathrm{i}vs}$ contains the transverse observation coordinate; W_z retains the propagation-distance dependence. Expanding that factor leads to the normalized even moments

$$M_{2j}(z) = \iint_{\widehat{\mathcal{D}}} s^{2j}W_z(s,t)\,ds\,dt, \qquad \mu_{2j}(z) = \frac{M_{2j}(z)}{M_0(z)}. \tag{41}$$

These are complex amplitude-weighted moments, retaining both Gaussian weighting and propagation phase. For the centered rectangular and circular pupils, every transmitting point (s,t) has a partner $(-s,t)$, and $W_z(-s,t) = W_z(s,t)$ because the exponent contains s^2. Opposite points therefore have equal complex weights but opposite odd powers of s. Integrating these pairs gives

$$M_{2j+1}(z) = \iint_{\widehat{\mathcal{D}}} s^{2j+1}W_z(s,t)\,ds\,dt = -M_{2j+1}(z) = 0. \tag{42}$$

The cancellation requires reflection symmetry of the weighted pupil, rather than a real-valued weight. The normalized field therefore becomes

$$\begin{aligned}\phi(v;z) &= \sum_{j=0}^{\infty}\frac{(-1)^j\mu_{2j}(z)v^{2j}}{(2j)!} \\ &= 1 - \frac{\mu_2(z)v^2}{2} + \frac{\mu_4(z)v^4}{24} + O(v^6).\end{aligned} \tag{43}$$

The removed observation phase remains outside the moment sum when reconstructing the dimensional field:

$$U_{\mathcal{D}}(x,0,z) = U_{\mathcal{D}}(0,0,z)e^{\mathrm{i}kx^2/(2z)}\phi(v;z). \tag{44}$$

Its modulus is one, so on a branch whose transverse principal maximum is at $x = 0$, the normalized intensity is $\mathrm{PSF}_x(x \mid 0,z) = |\phi(v;z)|^2$. Writing $\phi = Re^{\mathrm{i}\theta}$, with $R = |\phi|$, shows directly why intensity selects the real part of the logarithm:

$$\ln(\mathrm{PSF}_x) = \ln(|\phi|^2) = 2\ln(R) = 2\,\mathrm{Re}\{\ln(\phi)\}. \tag{45}$$

This identity holds wherever $\phi \neq 0$. The full field series is an identity on a bounded pupil; truncating it, or its logarithm, introduces an approximation. Expanding the natural logarithm is useful because a Gaussian intensity has an exactly quadratic logarithm, and the half-height condition becomes a low-degree polynomial in v^2. This retains the Gaussian limit while organizing departures from it into higher-order coefficients. With the logarithm chosen continuously from $\phi(0;z) = 1$, substitution of $\delta = \phi - 1$ into $\ln(1+\delta) = \delta - \delta^2/2 + \cdots$ gives

$$\begin{aligned}\ln\phi &= -\frac{\mu_2 v^2}{2} + \frac{\mu_4 - 3\mu_2^2}{24}v^4 + O(v^6),\\ \ln \mathrm{PSF}_x &= 2\,\mathrm{Re}\{\ln\phi\} = -A(z)v^2 - B(z)v^4 + O(v^6),\end{aligned} \tag{46}$$

where all moments are evaluated at the chosen z, and

$$A(z) = \mathrm{Re}\{\mu_2(z)\}, \qquad B(z) = \frac{\mathrm{Re}\{3\mu_2(z)^2 - \mu_4(z)\}}{12}. \tag{47}$$

The real part follows from the squared modulus; the complex moments are retained when forming their products. At PSF half height,

$$A(z)v_{1/2}^2 + B(z)v_{1/2}^4 = \ln 2, \qquad \mathrm{FWHM}_x(z) = \frac{\lambda z}{\pi a_0}v_{1/2}. \tag{48}$$

Set $T = v_{1/2}^2$, so the half-height equation is $BT^2 + AT - \ln 2 = 0$. For $A > 0$, the root connected to the second-order solution is

$$T = \frac{-A + \sqrt{A^2 + 4B\ln 2}}{2B} = \frac{2\ln 2}{A + \sqrt{A^2 + 4B\ln 2}} \longrightarrow \frac{\ln 2}{A} \quad (B \to 0). \tag{49}$$

The first quotient applies for $B \neq 0$; the rationalized form also supplies the finite $B = 0$ limit and avoids subtraction of nearly equal quantities. This choice follows the half-height root smoothly as the fourth-order correction is removed. Substitution into the dimensional width gives

$$\mathrm{FWHM}_x^{(4)}(z) \simeq \frac{\lambda z}{\pi a_0}\left[\frac{2\ln 2}{A(z) + \sqrt{A(z)^2 + 4B(z)\ln 2}}\right]^{1/2}. \tag{50}$$

The superscript denotes expansion order, not a fourth power. This is an explicit half-height solution once $A(z)$ and $B(z)$ have been evaluated from the pupil-moment integrals; explicit width does not imply that arbitrary-pupil coefficients are elementary functions. For a rectangle, the coefficients reduce to finite Gaussian or incomplete-gamma expressions. For a circle, they can be evaluated by one chord quadrature or by the analytical moment series developed below. This common expression uses the geometry-dependent moments of Eq. 41; replacing a_x by a alone does not replace those moments. It requires $M_0 \neq 0$, a central principal maximum, $A > 0$, and a real admissible half-height root. Evaluation at f, z_p or z_t gives the corresponding nominal-, peak- or minimum-plane estimate on a qualified central-lobe branch.

In particular, the pupil moments M_0, M_2, M_4 required for A and B can be computed with the same slice decomposition as the field. On the normalized chord, set $b = a_0^2\beta_x(z)$ and $h(t) = L(a_0 t)/a_0$. The strip function $S(b, 0; h)$ is Eq. 29 in dimensionless variables at zero transverse Fourier argument. Here b is the generally complex coefficient of the squared pupil coordinate. Differentiating with respect to that coefficient brings down the same coordinate powers needed in M_{2j}; the endpoints are held fixed. Thus

$$\left(-\frac{\partial}{\partial b}\right)^j S(b, 0; h) = \int_{-h}^{h} s^{2j} e^{-bs^2} ds = J_{2j}^{\mathrm{gen}}(b, h). \tag{51}$$

For example, $-\partial_b e^{-bs^2} = s^2 e^{-bs^2}$ generates J_2^{gen}, and $\partial_b^2 e^{-bs^2} = s^4 e^{-bs^2}$ generates J_4^{gen}. It is an analytical coefficient identity, not a requirement to approximate derivatives by finite differences. With $\hat{y} = y/a_0$, the remaining integration is

$$M_{2j}(z) = \int_{\hat{y}} e^{-a_0^2\beta_y(z)t^2} J_{2j}^{\mathrm{gen}}(a_0^2\beta_x(z), h(t))\, dt. \tag{52}$$

Rectangular separation leaves a ratio of constant-width strip moments; circular geometry integrates them over variable chords. The aperture-specific expressions follow below. Interval sums extend the same coefficient construction to pupils with gaps. The even-power simplification requires reflection symmetry of the full weighted pupil; otherwise odd moments must also be retained.

At a prescribed z, the expansion is local in the transverse coordinate about $x = 0$. Away from the focal lobe, the half-height crossing can lie beyond its accurate range even for a smooth central profile, producing order-unity thickness errors. A separate expansion of the width in z is additionally local to its axial expansion plane; neither approximation is justified at an axial half-intensity plane solely because it is accurate at the peak. Sixth- and eighth-order results improve the tested nominal and shifted-peak widths, but do not give uniform arbitrary-z accuracy. The complete strip or slice roots remain the reference for such planes. SI Section 4 gives the complete derivation and coefficient evaluations, and SI Section 4.3 gives the higher-order half-height equations and tested coverage.

For the axial FWHM in the strong-focus regime, we first approximate the on-axis field by its normalized focused-strip profile. Its real defocus parameter is

$$b_{\mathrm{ax}}(z) = \frac{ka_0^2}{2}\left(\frac{1}{z} - \frac{1}{f}\right). \tag{53}$$

Expanding the quadratic defocus factor $e^{\mathrm{i}b_{\mathrm{ax}}s^2}$ in b_{ax} produces moments of s^2. In contrast, the transverse-FWHM construction at fixed z expands the Fourier phase factor $e^{-\mathrm{i}vs}$ in $v = ka_0x/z$, the dimensionless transverse spatial-frequency variable. The complex inner-strip coefficient above combines Gaussian weighting and this phase as $b = a_0^2/w_x^2 - \mathrm{i}b_{\mathrm{ax}}$. The axial reduction assumes slow variation of the propagation prefactor and non-focused contribution across the focal lobe; it is derived in Section 3.4 and applied to the circular central-chord limit in Section 3.5. Its physical reduction and accuracy are distinct from the transverse formula above. SI Section 4.5 gives the complete axial derivation and comparison.

3.4 Rectangular pupil: complete separable solutions

3.4.1 Governing field and definitions

For the rectangular pupil, set $\mathcal{D} = \mathcal{D}_{\mathrm{rect}}$ and $L(y') = a_x$ in Eq. 33. Both the domain and amplitude are separable. To identify the rectangular factors locally, write

$$\beta_x^{(R)} = \beta_x, \qquad \beta_y^{(R)} = \beta_y, \tag{54}$$

and factor the complete finite-distance field as

$$U_{\mathrm{rect}}(x, y, z) = C(x, y, z)A_0U_x(x, z)U_y(y, z), \tag{55}$$

$$U_x = \int_{-a_x}^{a_x} e^{-\beta_x^{(R)}x'^2 - \mathrm{i}q_xx'}\,dx', \qquad U_y = \int_{-a_y}^{a_y} e^{-\beta_y^{(R)}y'^2 - \mathrm{i}q_yy'}\,dy'. \tag{56}$$

Both factors are the strip function introduced in Section 3.2.

For the rectangular Gaussian/top-hat family, Eq. 21 factorizes exactly:

$$U_{\mathrm{rect}}(x, y, z) = CA_0S(\beta_x^{(R)}, q_x; a_x)S(\beta_y^{(R)}, q_y; a_y), \tag{57}$$

where the common coefficients in Eq. 23 retain the independent incident radii w_x, w_y. This is the complete rectangular field throughout the three-dimensional paraxial focal region. Its invariant-axis limit contains the established cylindrical-lens result [6].

At fixed (y, z), the factors $U_y(y, z)$ and $|C| = 1/(\lambda z)$ are independent of x. Dividing intensities at the same (y, z) therefore gives, wherever the denominator is nonzero,

$$\frac{I_{\mathrm{rect}}(x, y, z)}{I_{\mathrm{rect}}(0, y, z)} = \frac{|CA_0|^2|U_x(x, z)|^2|U_y(y, z)|^2}{|CA_0|^2|U_x(0, z)|^2|U_y(y, z)|^2} = \left|\frac{U_x(x, z)}{U_x(0, z)}\right|^2. \tag{58}$$

The cancellation holds for finite a_y, w_y as well as their limiting cases. These parameters still determine absolute intensity and axial evolution. On a central-principal-maximum branch at $y = 0$, the transverse profile and its first positive half-height root satisfy

$$\mathrm{PSF}_x(x \mid 0, z) = \left| \frac{S(\beta_x, kx/z; a_x)}{S(\beta_x, 0; a_x)} \right|^2, \qquad \mathrm{PSF}_x(x_{1/2} \mid 0, z) = \frac{1}{2}, \qquad \mathrm{FWHM}_x(z) = 2x_{1/2}(z). \tag{59}$$

At fixed (y, z), the multiplicative non-focused factor $S(\beta_y^{(R)}, q_y; a_y)$ cancels from the locally normalized focused-x profile and therefore from its transverse FWHM. It does not cancel from on-axis propagation. The exact finite-pupil intensity is

$$I_{\mathrm{rect}}(0, 0, z) \propto \frac{1}{z^2} \left| S(\beta_x^{(R)}, 0; a_x) S(\beta_y^{(R)}, 0; a_y) \right|^2, \tag{60}$$

so both strip factors and the propagation prefactor enter z_p and the axial FWHM. For a smooth selected axial lobe, differentiate the complex field before taking the real part:

$$\frac{dI_{\mathrm{ax}}}{dz} = 2\,\mathrm{Re}\left\{ U_{\mathrm{ax}}^* \frac{dU_{\mathrm{ax}}}{dz} \right\}, \qquad I'_{\mathrm{ax}}(z_p) = 0, \quad I''_{\mathrm{ax}}(z_p) < 0. \tag{61}$$

The neighboring half-height crossings then give

$$I_{\mathrm{ax}}(z_\pm) = \frac{1}{2} I_{\mathrm{ax}}(z_p), \qquad \mathrm{FWHM}_z = z_+ - z_-, \qquad 0 < z_- < z_p < z_+. \tag{62}$$

The same root construction applies to the circular field below. Oscillatory broad profiles use the peak and width convention of Section 2.3; the derivative identity refers to the raw field.

This field-to-width relation includes the nominal and displaced focal planes. The following illumination limits simplify either the profile itself or its half-height equation.

3.4.2 Top-hat illumination: transverse and axial FWHMs

At $z = f$, $\beta_x^{(R)} = 0$ and Eq. 32 gives the exact normalized focused-x profile

$$\frac{U_{\mathrm{rect}}(x, y, f)}{U_{\mathrm{rect}}(0, y, f)} = e^{\mathrm{i}kx^2/(2f)} \,\mathrm{sinc}\left(\frac{ka_x x}{f} \right), \qquad \frac{I_{\mathrm{rect}}(x, y, f)}{I_{\mathrm{rect}}(0, y, f)} = \mathrm{sinc}^2\left(\frac{ka_x x}{f} \right), \tag{63}$$

The observation-only quadratic phase is retained in the complex-field ratio and cancels from intensity. The positive half-maximum root satisfies $(\sin(v)/v)^2 = 1/2$ with $v_{1/2} = 1.391557378\ldots$. Doubling $x_{1/2} = v_{1/2} f/(ka_x)$ gives

$$\mathrm{FWHM}_{x,f}^{\mathrm{rect,TH}} = 0.88589294 \frac{\lambda f}{D_x}, \qquad D_x = 2a_x. \tag{64}$$

For the rectangular pupil, the strong-focus approximation assumes that the non-focused contribution and propagation prefactor vary slowly across the focal lobe, as in the invariant-axis limit. The remaining normalized focused factor is $\frac{1}{2}\int_{-1}^{1} e^{\mathrm{i}us^2/2} ds$, with $u = ka_x^2(1/z - 1/f)$. Its half-intensity root is $u_{1/2} = 5.460003874599\ldots$, giving

$$\mathrm{FWHM}_z^{\mathrm{rect,TH}} \simeq 1.73797321 \frac{\lambda}{\mathrm{NA}_{\mathrm{geom}}^2}, \qquad \mathrm{NA}_{\mathrm{geom}} \simeq \frac{a_x}{f}. \tag{65}$$

The two symmetric axial half crossings follow from $|\frac{1}{2}\int_{-1}^{1} e^{\mathrm{i}us^2/2} ds|^2 = 1/2$ and the first positive root $u_{1/2} = 5.460003874599\ldots$. Linearizing $1/z$ about $1/f$ gives Eq. 65. This coefficient is not the exact axial width of every finite rectangular stop: in the verified square-pupil cases it differs from Eq. 60 by about 5–7% for $N_a = 10$–100, but by 37% or more at $N_a \leq 3$. SI Section 5 gives the step-by-step transverse and axial derivations, exact finite-stop roots, and the $z_p \neq f$ case.

3.4.3 Untruncated Gaussian illumination: transverse and axial FWHMs

When $a_x, a_y \to \infty$, each strip tends to $S(\beta, q; \infty) = \sqrt{\pi/\beta}\exp[-q^2/(4\beta)]$. Substitution in the fixed-plane ratio of Eq. 59 gives a Gaussian intensity profile. At its positive half-height coordinate,

$$\mathrm{PSF}_{x,G}(x_{1/2}; z) = \exp\left[-\frac{k^2 x_{1/2}^2}{2z^2}\,\mathrm{Re}\left\{\frac{1}{\beta_x^{(R)}}\right\}\right] = \frac{1}{2}. \tag{66}$$

Taking its natural logarithm and using $\mathrm{FWHM}_x = 2x_{1/2}$ gives

$$\mathrm{FWHM}_x^G(z) = \frac{\lambda z}{\pi}\sqrt{\frac{2\ln 2}{\mathrm{Re}\{1/\beta_x^{(R)}\}}}, \qquad \mathrm{FWHM}_{x,f}^G = \sqrt{2\ln 2}\,\frac{\lambda f}{\pi w_x}. \tag{67}$$

This width follows directly from the exact Gaussian integral. The moment framework gives the same result because the Gaussian log-intensity is exactly quadratic. To expose the propagation dependence, substitute $\beta_x = w_x^{-2} - \mathrm{i}k(1/z - 1/f)/2$. Its reciprocal has real part $w_x^{-2}/[w_x^{-4} + k^2(1/z - 1/f)^2/4]$, giving the exact Gaussian width

$$\left[\mathrm{FWHM}_x^G(z)\right]^2 = 2\ln 2\left[w_x^2\left(1 - \frac{z}{f}\right)^2 + \left(\frac{\lambda z}{\pi w_x}\right)^2\right]. \tag{68}$$

The two terms describe geometrical convergence and diffraction broadening. Differentiating their sum gives the minimum plane and thickness:

$$\frac{z_{t,G}}{f} = \frac{s_x^2}{1 + s_x^2}, \qquad \mathrm{FWHM}_{x,t}^G = \frac{\sqrt{2\ln 2}\,w_x}{\sqrt{1 + s_x^2}}, \qquad s_x = \frac{\pi w_x^2}{\lambda f}. \tag{69}$$

These transverse results are exact throughout the Gaussian Fresnel field. The axial intensity retains both infinite-strip factors in Eq. 60, so its peak need not coincide with $z_{t,G}$. For equal incident radii, its peak and half-height equations are the cubic and quartic equations developed with the circular Gaussian limit below; for unequal radii the same product construction retains w_x and w_y separately. When the non-focused Gaussian radius changes slowly across the focal interval, the axial intensity is proportional to the reciprocal focused radius. Completing the square in Eq. 68 gives its waist form, with output Rayleigh length $z_{RG} = f s_x/(1+s_x^2)$, and hence

$$\frac{I_G(z)}{I_G(z_{t,G})} \simeq \left[1 + \left(\frac{z - z_{t,G}}{z_{RG}}\right)^2\right]^{-1/2}, \qquad z_\pm \simeq z_{t,G} \pm \sqrt{3} z_{RG} \tag{70}$$

at half intensity. Subtracting these crossings and then taking $s_x \gg 1$ gives

$$\mathrm{FWHM}_z^G \simeq 2\sqrt{3} z_{RG} \simeq \frac{2\sqrt{3}\lambda f^2}{\pi w_x^2}. \tag{71}$$

The half-height construction and the complete Gaussian axial product are derived in SI Section 5.2. Both crossings must lie at positive z; slow variation of the non-focused radius and strong focusing remain the conditions of the last axial approximation.

3.4.4 Truncated Gaussian illumination: profiles and FWHM roots

For finite $\tau_x = a_x/w_x$, set $s = x'/a_x$ and $v = k a_x x/f$. At $z = f$, the focused quadratic propagation and lens phases cancel, so $\beta_x = 1/w_x^2$. The substitution gives

$$\beta_x x'^2 = \frac{a_x^2}{w_x^2} s^2 = \tau_x^2 s^2, \qquad q_x x' = \frac{kx}{f} a_x s = v s. \tag{72}$$

The endpoints become $s = \pm 1$ and $dx' = a_x ds$, so

$$S(\beta_x, kx/f; a_x) = a_x \int_{-1}^{1} e^{-\tau_x^2 s^2 - \mathrm{i}vs} ds = a_x S(\tau_x^2, v; 1). \tag{73}$$

On normalization, a_x and the non-focused factor cancel, leaving

$$\phi_R(v) = \frac{S(\tau_x^2, v; 1)}{S(\tau_x^2, 0; 1)}, \qquad |\phi_R(v_{1/2})|^2 = \frac{1}{2}, \qquad \mathrm{FWHM}_{x,f}^{\mathrm{rect}} = \frac{\lambda f}{\pi a_x} v_{1/2}. \tag{74}$$

This is a one-dimensional root of a known error-function expression. For the axial width, retain both strip factors in Eq. 60 and determine the selected peak and connected half-height crossings from Eqs. 61–62. The strong-focus strip profile and explicit moment alternatives are developed in Section 3.4.5; SI Section 5.2 gives the complete finite-truncation derivation.

3.4.5 Moment-based FWHM formulas -- all regimes

The common moment approximation of Section 3.3 gives an explicit alternative. Gaussian truncation enters the coefficients continuously, covering top-hat, finite-Gaussian and untruncated-Gaussian illumination. The transverse expressions below use the nominal plane; the compact axial expressions additionally use a strong-focus reduction.

Transverse moment width. At nominal focus, the rectangular moments are real and the non-focused moment factor cancels, leaving

$$\mu_{2j}^{\mathrm{rect}}(f) = \frac{J_{2j}(\tau_x, 1)}{J_0(\tau_x, 1)}, \qquad J_{2j}(\tau, h) = J_{2j}^{\mathrm{gen}}(\tau^2, h). \tag{75}$$

The first argument of $J_{2j}(\tau, h)$ is the truncation ratio, whereas $J_{2j}^{\mathrm{gen}}(b, h)$ uses the quadratic exponent coefficient. At nominal focus these are related by $b = \tau^2$. Using evenness to integrate over $0 \le s \le h$ and substituting $u = \tau^2 s^2$ gives

$$J_{2j}(\tau, h) = \int_{-h}^{h} s^{2j} e^{-\tau^2 s^2} ds = \begin{cases} \tau^{-2j-1} \gamma(j + \frac{1}{2}, \tau^2 h^2), & \tau > 0, \\ 2h^{2j+1}/(2j+1), & \tau = 0, \end{cases} \qquad j = 0, 1, 2, \ldots, \tag{76}$$

where γ is the lower incomplete gamma function. Thus the rectangular coefficients are explicit special-function expressions, with a continuous top-hat limit. In particular, inserting $j = 1, 2$ and dividing by J_0 gives, for $\tau_x > 0$,

$$\begin{aligned} \mu_2 &= \frac{1}{2\tau_x^2} - \frac{e^{-\tau_x^2}}{\sqrt{\pi}\tau_x \operatorname{erf}(\tau_x)}, \\ \mu_4 &= \frac{3}{4\tau_x^4} - \frac{(2\tau_x^2 + 3)e^{-\tau_x^2}}{2\sqrt{\pi}\tau_x^3 \operatorname{erf}(\tau_x)}. \end{aligned} \tag{77}$$

For these real nominal-plane moments, Eq. 47 reduces to

$$A = \mu_2, \qquad B = \frac{3\mu_2^2 - \mu_4}{12}. \tag{78}$$

At $\tau_x = 0$, direct integration of the uniform amplitude weight gives

$$\mu_2 = \frac{1}{3}, \qquad \mu_4 = \frac{1}{5}, \qquad A = \frac{1}{3}, \qquad B = \frac{1}{90}. \tag{79}$$

Equations 77–79 specify the coefficients for positive truncation and its top-hat limit without pupil quadrature. SI Section 5.2 gives the small-τ_x series used to avoid subtractive cancellation when evaluating these limits. Substitution into the common half-height solution, Eq. 50, yields

$$\mathrm{FWHM}_{x,f}^{\mathrm{rect}} \simeq \frac{\lambda f}{\pi a_x}\left[\frac{2\ln 2}{A+\sqrt{A^2+4B\ln 2}}\right]^{1/2}. \tag{80}$$

The moments retain every finite τ_x, and the expression recovers the exact Gaussian nominal width as the stop becomes ineffective. Its existing 124-case comparison gives a maximum sampled error of 0.411%. The axial counterpart starts instead from Eq. 60; retaining both strips gives the complete root solution, while the following reduction supplies a compact moment formula near focus. The detailed derivations and the dependence on rectangular aspect ratio are given in SI Section 5.

Explicit axial width in the strong-focus regime. The focused-strip profile underlying Eq. 65 also admits a moment approximation for finite Gaussian truncation. To write the shared strip calculation, use $a = a_x$ and $\tau = \tau_x = a_x/w_x$ for the rectangle. The same expressions will be used for the circular central-chord approximation with a the pupil radius and $\tau = a/w_L$; that additional geometrical reduction is derived in Section 3.5.4. With $b = u/2$, the normalized focused-strip field is

$$\psi(b) = \frac{\int_{-1}^{1} e^{-\tau^2 s^2} e^{\mathrm{i}bs^2}\, ds}{\int_{-1}^{1} e^{-\tau^2 s^2}\, ds}, \qquad b = \frac{ka^2}{2}\left(\frac{1}{z}-\frac{1}{f}\right). \tag{81}$$

Here $\psi(b)$ is a dimensionless normalized complex field, while $|\psi(b)|^2$ is its dimensionless normalized intensity. The real parameter b measures axial defocus, with $b = 0$ at $z = f$. The positive amplitude weight makes the intensity maximal at zero defocus. Define its first positive half-intensity root by

$$\psi(0) = 1, \qquad |\psi(b_{1/2})|^2 = \frac{1}{2}, \qquad b_{1/2} > 0. \tag{82}$$

Thus $b_{1/2}$ is a dimensionless defocus coordinate; conversion to z supplies a physical axial extent. For this one-dimensional profile, use the real strip moments $\mu_{2j} = J_{2j}(\tau,1)/J_0(\tau,1)$ from Eq. 76. They describe the positive Gaussian amplitude on the focused strip; the complete circular pupil generally has complex moments. The variance and fourth cumulant of s^2 under the normalized amplitude weight are

$$\begin{aligned} V &= \mu_4 - \mu_2^2, \\ \kappa_4 &= \mu_8 - 4\mu_6\mu_2 - 3\mu_4^2 + 12\mu_4\mu_2^2 - 6\mu_2^4. \end{aligned} \tag{83}$$

The even cumulants give $\ln|\psi|^2 = -Vb^2 + \kappa_4 b^4/12 + O(b^6)$. Expanding the inverse square of intensity then gives

$$|\psi|^{-4} \simeq 1 + 2Vb^2 + Cb^4, \qquad C = 2V^2 - \kappa_4/6, \tag{84}$$

where C here denotes the quartic coefficient of this normalized profile. All required moments are explicit: with $T = \tau^2 > 0$, $E = e^{-\tau^2}/[\sqrt{\pi}\tau\,\mathrm{erf}(\tau)]$ and $\mu_0 = 1$,

$$\mu_{2j} = \frac{2j-1}{2T}\mu_{2j-2} - E, \qquad V = \frac{1}{2T^2} - E\left(1+\frac{1}{2T}\right) - E^2. \tag{85}$$

The recurrence supplies $\mu_2, \mu_4, \mu_6, \mu_8$ for Eq. 83; the fully expanded expression for C and stable small-τ evaluation are in SI Section 4.5.2. The same explicit pair V, C is written for the circular central-chord case in Section 3.5.5, with the appropriate aperture and truncation definitions. Direct integration at zero truncation and the infinite-Gaussian integral give

$$(V,C) = \begin{cases} (4/45, 16/945), & \tau = 0 \quad \text{(top-hat)}, \\ (1/(2\tau^4), 0), & \text{untruncated-Gaussian limit}. \end{cases} \tag{86}$$

These coefficients are shared by the rectangular focused strip and the circular central-chord reduction; their complete-field reduction errors remain geometry dependent. This form recovers the untruncated-Gaussian strip exactly. At half intensity, $|\psi|^{-4} = 4$; solving the quadratic in b^2 and linearizing $1/z$ about $1/f$ yields

$$b_{1/2} \simeq \left[\frac{3}{V+\sqrt{V^2+3C}}\right]^{1/2}, \qquad \mathrm{FWHM}_z \simeq \frac{2\lambda f^2}{\pi a^2} b_{1/2}. \tag{87}$$

Positive variance and a real, admissible positive root are required. In the untruncated-Gaussian limit, $V = 1/(2\tau^4)$ and $C = 0$, giving $b_{1/2} = \sqrt{3}\tau^2$ and, for the rectangle, $\mathrm{FWHM}_z \simeq 2\sqrt{3}\lambda f^2/(\pi w_x^2)$, in agreement with Eq. 71. For the round Gaussian, $w_x = w_L$. Over the 124 tested strip truncations, the maximum relative error in $b_{1/2}$ is 12.60%; this measures the approximation to the strip root. SI Section 4 gives the complete derivation and sampled errors.

A more accurate explicit interpolation retains only μ_2 and μ_4 and fixes both limiting widths. Define the moment-shape parameter

$$\chi = \frac{5\mu_4/\mu_2^2 - 9}{6}, \qquad c_{\mathrm{TH}} = 0.9100006458, \qquad c_G = \frac{\sqrt{3}}{2}. \tag{88}$$

For the truncated-Gaussian amplitude family, χ changes from zero in the top-hat limit to one in the untruncated limit. The calibrated interpolation is

$$\begin{aligned} b_{1/2}^{\mathrm{cal}} &= \frac{(1-\chi)c_{\mathrm{TH}} + \chi c_G + \chi(1-\chi)q(\chi)}{\mu_2}, \\ q(\chi) &= -0.4231078677 - 0.5290236236\chi + 0.8983447672\chi^2, \\ \mathrm{FWHM}_z^{\mathrm{cal}} &\simeq \frac{2\lambda f^2}{\pi a^2} b_{1/2}^{\mathrm{cal}}. \end{aligned} \tag{89}$$

Its three fitted coefficients give a maximum strip-root error of 0.768% on 605 independent validation points spanning $0 \le \tau \le 12$. The endpoints are fixed to the known top-hat and Gaussian limits; the intervening accuracy is numerical evidence for this amplitude family. Both axial formulas use the same physical strong-focus reduction. Their additional complete-field error is assessed for the derived and calibrated expressions in SI Figure 12 and SI Figure 13, with separate tests for peak location, numerical refinement and regression sensitivity. The calibrated expression improves the strip-profile approximation; its practical input domain is determined by the complete-field width comparison.

Applying Eq. 87 to a finite pupil also uses a near-focus reduction of the complete field: the non-focused contribution, propagation prefactor and circular chord dependence affect the physical width. The dimensionless half-extent $\epsilon_z = b_{1/2}/(\pi N_a)$ measures the linearization scale of $b = \pi N_a(f/z-1)$; the formal narrow-lobe limit is $\epsilon_z \ll 1$. For a rectangular stop N_a uses a_x, while for an effectively untruncated Gaussian $\epsilon_z \simeq \sqrt{3}/(\pi N_G)$. The practical comparison also retains broader near-centered lobes and measures their formula error directly. The strip-profile errors compare the derived or calibrated $b_{1/2}$ with a numerical root of the same $|\psi(b)|^2$. Replacing the complete axial intensity by this focused-strip profile introduces a separate physical reduction error. For a rectangle the exact separation is

$$\frac{I_{\mathrm{rect}}(z)}{I_{\mathrm{rect}}(f)} = \left(\frac{f}{z}\right)^2 \left|\frac{S(\beta_y(z), 0; a_y)}{S(\beta_y(f), 0; a_y)}\right|^2 |\psi[b(z)]|^2. \tag{90}$$

The factors preceding $|\psi|^2$ can shift the peak and change its physical width; the circular central-chord approximation additionally simplifies the variable pupil boundary. Retaining $z = f/[1 + b/(\pi N_a)]$ gives the exact conversion of the two symmetric reduced-strip roots to $z_- = f/(1+\epsilon_z)$ and $z_+ = f/(1-\epsilon_z)$ when $\epsilon_z < 1$. Their separation is $2f\epsilon_z/(1-\epsilon_z^2)$, rather than the linearized $2f\epsilon_z$. This conversion preserves the symmetric reduced strip profile but does not restore the omitted factors of the complete field. SI Section 4.5.4 derives the conversion and measures the separate error contributions.

3.5 Circular pupil: Cartesian aperture-slice decomposition

3.5.1 Governing field and definitions

For the circular illumination family, set $\mathcal{D} = \mathcal{D}_{\mathrm{circ}}$ and $w_x = w_y = w_L$ in Eqs. 23–24, so that $U_{\mathcal{D}} = U_{\mathrm{circ}}$ and both real inverse-radius terms become $1/w_L^2$. The common slice formulation now uses the variable chord of Eq. 27. The disk inequality $x'^2 + y'^2 \le a^2$ gives $|y'| \le a$ and, at each fixed y', the focused-coordinate interval

$$-L(y') \le x' \le L(y'), \qquad L(y') = \sqrt{a^2 - y'^2}. \tag{91}$$

Figure 4 illustrates this circular slice geometry: the radius a and slice height y' determine the chord half-width $L(y')$. Substituting these limits into Eq. 24 first gives

$$U_{\mathrm{circ}} = CA_0 \int_{-a}^{a} e^{-\beta_y y'^2 - \mathrm{i}q_y y'} \left[\int_{-L(y')}^{L(y')} e^{-\beta_x x'^2 - \mathrm{i}q_x x'} dx' \right] dy'. \tag{92}$$

The inner integral has exactly the strip form of Eq. 29, but with a half-width determined by the outer coordinate. Thus

$$U_{\mathrm{circ}}(x, y, z) = CA_0 \int_{-a}^{a} e^{-\beta_y y'^2 - \mathrm{i}q_y y'} S(\beta_x, q_x; L(y'))\, dy'. \tag{93}$$

Explicitly, for $\beta_x \neq 0$ the chord contribution is

$$S(\beta_x, q_x; L) = \frac{\sqrt{\pi}\, e^{-q_x^2/(4\beta_x)}}{2\sqrt{\beta_x}} \left[\mathrm{erf}\left(\sqrt{\beta_x} L + \frac{\mathrm{i}q_x}{2\sqrt{\beta_x}} \right) + \mathrm{erf}\left(\sqrt{\beta_x} L - \frac{\mathrm{i}q_x}{2\sqrt{\beta_x}} \right) \right], \qquad L = \sqrt{a^2 - y'^2}. \tag{94}$$

Its continuous $\beta_x = 0$ value is $2L\,\mathrm{sinc}(q_x L)$, including $2L$ at $q_x = 0$.

Thus the physical two-dimensional pupil integral becomes one exact numerical quadrature without replacing the circular stop by a slit. Integration over the focused pupil coordinate is analytical; only the non-focused pupil coordinate remains numerical. The field remains nonseparable because the strip half-width depends on y'.

For the xz axial-propagation plane, set $y = 0$, so $q_y = 0$ and the outer integrand is even. Retaining the incident amplitude and the full propagation prefactor gives the unnormalized dimensional field

$$U_{\mathrm{circ}}(x, 0, z) = \frac{2A_0 e^{\mathrm{i}kz + \mathrm{i}kx^2/(2z)}}{\mathrm{i}\lambda z} \int_0^a e^{-\beta_y y'^2} S\left(\beta_x, \frac{kx}{z}; \sqrt{a^2 - y'^2} \right) dy'. \tag{95}$$

Setting $x = 0$ then gives the optical-axis field

$$U_{\mathrm{circ}}(0, 0, z) = \frac{2A_0 e^{\mathrm{i}kz}}{\mathrm{i}\lambda z} \int_0^a e^{-\beta_y y'^2} S\left(\beta_x, 0; \sqrt{a^2 - y'^2} \right) dy', \tag{96}$$

where the zero-transverse-frequency chord simplifies to

$$S(\beta_x, 0; L) = \begin{cases} \frac{\sqrt{\pi}}{\sqrt{\beta_x}} \mathrm{erf}(\sqrt{\beta_x} L), & \beta_x \neq 0, \\ 2L, & \beta_x = 0. \end{cases} \tag{97}$$

Their squared moduli supply the xz-plane and on-axis intensity profiles. Transverse normalization at a fixed z removes the observation-only phase and common amplitude factor; axial peak and width calculations retain the physical $1/z^2$ intensity factor. These expressions apply to finite Gaussian truncation and its top-hat limit; the dimensionless forms below are obtained by scaling the same fields.

With $t = y'/a$ and Eqs. 16–17, define

$$B_x = \tau^2 - \mathrm{i}\pi N_a(\tilde{z}^{-1} - 1), \qquad B_y = \tau^2 - \mathrm{i}\pi N_a \tilde{z}^{-1}, \tag{98}$$

$$Q_x = \frac{2\pi\tilde{x}}{\tilde{z}}, \qquad Q_y = \frac{2\pi\tilde{y}}{\tilde{z}}. \tag{99}$$

Apart from the incident amplitude and a unit-modulus observation phase,

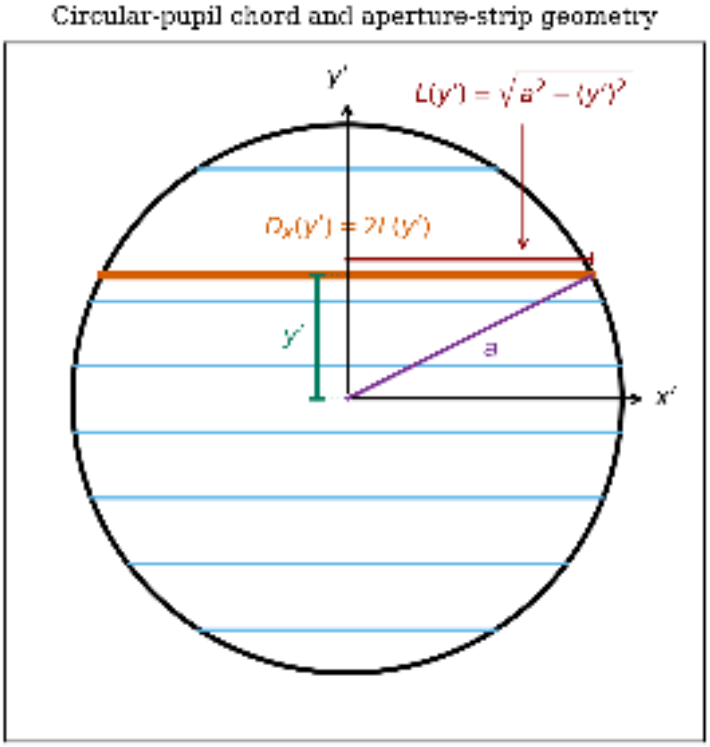


Figure 4: Cartesian aperture-slice geometry. Integration over the focused pupil coordinate x' is analytical for each chord; integration over y' remains numerical. The orange chord has width $D_x(y') = 2L(y')$. The purple radius a and green height y' determine the half-width $L(y') = \sqrt{a^2 - y'^2}$, indicated by the dark-red expression, leader and bracket over the right half of the chord.

$$\widetilde{U}_{\text{circ}}(\tilde{x},\tilde{y},\tilde{z}) = \frac{N_a}{\tilde{z}} \int_{-1}^{1} e^{-B_y t^2 - \mathrm{i}Q_y t} S\big(B_x, Q_x; \sqrt{1-t^2}\big)\, dt. \tag{100}$$

Equation 100 is the same physical field in scaled variables, useful for parameter comparisons, maps and the analytical series below. Specifically, $U_{\text{circ}} = (A_0/\mathrm{i})e^{\mathrm{i}kz + \mathrm{i}k(x^2+y^2)/(2z)}\widetilde{U}_{\text{circ}}$; the $N_a/\tilde{z}$ factor remains essential for axial intensity. At $\tilde{y} = 0$, evenness gives the axial-propagation-plane and optical-axis restrictions

$$\widetilde{U}_{\text{circ}}(\tilde{x},0,\tilde{z}) = \frac{2N_a}{\tilde{z}} \int_{0}^{1} e^{-B_y t^2} S\left(B_x, \frac{2\pi\tilde{x}}{\tilde{z}}; \sqrt{1-t^2}\right) dt, \tag{101}$$

$$\widetilde{U}_{\text{circ}}(0,0,\tilde{z}) = \frac{2N_a}{\tilde{z}} \int_{0}^{1} e^{-B_y t^2} S\big(B_x, 0; \sqrt{1-t^2}\big)\, dt. \tag{102}$$

At nominal focus, $\tilde{z} = 1$, $B_x = \tau^2$, $B_y = \tau^2 - \mathrm{i}\pi N_a$, and $Q_{x,y} = 2\pi\tilde{x}, 2\pi\tilde{y}$. The following limits are most transparent in these scaled variables; the final widths are converted back to physical lengths. Since $N_a = a^2/(\lambda f)$, small and large N_a compare a^2 with λf. At fixed λ, f, they correspond to aperture radii small or large relative to $\sqrt{\lambda f}$; this is distinct from the paraxial condition. A top-hat follows by $\tau \to 0$ at fixed aperture. Expanding the stop at fixed Gaussian radius instead gives $\tau \to \infty$ and $N_a = \tau^2 N_G$ with fixed N_G.

3.5.2 Top-hat illumination: transverse and axial FWHMs

Set $\tau = 0$, or equivalently $w_L^{-2} = 0$, and consider $y = 0, z = f$. The focused quadratic phase cancels: $\beta_x = 0$, $\beta_y = -\mathrm{i}k/(2f)$ and $q_x = kx/f$. With $s = x'/a$, $t = y'/a$, $h(t) = \sqrt{1-t^2}$ and $v = aq_x = kax/f = 2\pi\tilde{x}$, restoring the focused-coordinate integration in Eq. 100 gives

$$\begin{aligned}\widetilde{U}^{\mathrm{TH}}_{\mathrm{circ}}(\tilde{x},0,1) &= N_a\int_{-1}^{1} e^{\mathrm{i}\pi N_a t^2}\left[\int_{-h(t)}^{h(t)} e^{-\mathrm{i}vs}ds\right]dt \\ &= N_a\int_{-1}^{1} e^{\mathrm{i}\pi N_a t^2}2h(t)\,\mathrm{sinc}[vh(t)]dt.\end{aligned} \tag{103}$$

The sinc factor is the integrated x' contribution, not a replacement of the circular pupil by a fixed slit. The exact nominal-plane PSF is

$$\mathrm{PSF}_x(x\mid 0,f) = \left|\frac{U^{\mathrm{TH}}_{\mathrm{circ}}(x,0,f)}{U^{\mathrm{TH}}_{\mathrm{circ}}(0,0,f)}\right|^2 = \left|\frac{\int_{-1}^{1} e^{\mathrm{i}\pi N_a t^2}h(t)\,\mathrm{sinc}[vh(t)]dt}{\int_{-1}^{1} e^{\mathrm{i}\pi N_a t^2}h(t)dt}\right|^2. \tag{104}$$

The common N_a prefactor and the unit-modulus observation phase cancel on normalization, while the N_a-dependent non-focused pupil phase remains inside the integrals. To derive the small-N_a limit, use $s=\rho\cos\theta$, $t=\rho\sin\theta$, where $\rho=r/a$ is the pupil radius scaled by a. The unit disk has $0\le\rho\le 1$, $0\le\theta<2\pi$, and Jacobian $ds\,dt=\rho\,d\rho\,d\theta$. The same field becomes

$$\widetilde{U}^{\mathrm{TH}}_{\mathrm{circ}}(\tilde{x},0,1) = N_a\int_0^1\int_0^{2\pi} e^{\mathrm{i}\pi N_a\rho^2\sin^2\theta}e^{-\mathrm{i}v\rho\cos\theta}\rho\,d\theta\,d\rho. \tag{105}$$

For $\pi N_a \ll 1$, the first phase is uniformly small over the pupil. Its exponential tends to one, leaving the polar form of the transverse Fourier factor $e^{-\mathrm{i}q_x x'}$. The angular and radial integrations are

$$\int_0^{2\pi} e^{-\mathrm{i}v\rho\cos\theta}d\theta = 2\pi J_0(v\rho), \qquad 2\pi\int_0^1 \rho J_0(v\rho)d\rho = \frac{2\pi J_1(v)}{v}. \tag{106}$$

The radial step follows from $d[\rho J_1(v\rho)]/d\rho = v\rho J_0(v\rho)$ and has continuous value π at $v=0$. Thus

$$\widetilde{U}^{\mathrm{TH}}_{\mathrm{circ}} \simeq \pi N_a\frac{2J_1(v)}{v}, \qquad \lim_{N_a\to 0}\mathrm{PSF}_x(x\mid 0,f) = \left|\frac{2J_1(v)}{v}\right|^2 \quad \text{at fixed } v. \tag{107}$$

The equality identifies the limiting PSF. At finite N_a, Eq. 104 retains the residual pupil phase and gives the complete normalized profile.

For large aperture Fresnel number N_a, the non-focused phase in Eq. 103 oscillates rapidly. In physical coordinates it is $\varphi(y') = ky'^2/(2f)$, with $\varphi'(y') = ky'/f$: its only interior stationary point is $y'=0$. Contributions away from that point largely cancel. Expanding the chord factor about $L(0)=a$ and retaining its leading value gives the central-chord contribution. The remaining local oscillatory Gaussian integral is

$$\int_{-\infty}^{\infty} e^{\mathrm{i}ky'^2/(2f)}dy' = e^{\mathrm{i}\pi/4}\sqrt{\frac{2\pi f}{k}} = e^{\mathrm{i}\pi/4}\sqrt{\lambda f}. \tag{108}$$

This integral is understood in the oscillatory sense, or as the limit with a positive Gaussian damping factor. The domain extension is part of the leading stationary-phase approximation, justified for fixed v on the central-lobe scale. SI Section 6.3 derives the method, the endpoint contributions and its application here. Consequently,

$$\widetilde{U}^{\mathrm{TH}}_{\mathrm{circ}} \simeq 2\sqrt{N_a}\,e^{\mathrm{i}\pi/4}\,\mathrm{sinc}(v), \qquad \lim_{N_a\to\infty}\mathrm{PSF}_x(x\mid 0,f) = \mathrm{sinc}^2(v) \quad \text{at fixed } v. \tag{109}$$

The common stationary-phase multiplier cancels in the normalized intensity. At finite N_a, the complete integral over the circular pupil, equivalently the variable-chord expression in Eq. 103, retains the corrections to this limit.

The first positive half-height roots and the conversion from scaled position to physical full width are

$$\begin{aligned}
\left|\frac{2J_1(v_{1/2})}{v_{1/2}}\right|^2 = \frac{1}{2} \quad &\Rightarrow \quad v_{1/2} = 1.616339948\ldots \quad (N_a \to 0),\\
\mathrm{sinc}^2(v_{1/2}) = \frac{1}{2} \quad &\Rightarrow \quad v_{1/2} = 1.391557378\ldots \quad (N_a \to \infty),\\
\mathrm{FWHM}_{x,f}^{\mathrm{circ,TH}} &= 2x_{1/2} = \frac{\lambda f}{\pi a} v_{1/2}.
\end{aligned} \tag{110}$$

Substituting these roots gives

$$\mathrm{FWHM}_{x,f}^{\mathrm{circ,TH}} \sim \begin{cases} 1.02899397\,\lambda f/D_a, & N_a \to 0,\\ 0.88589294\,\lambda f/D_a, & N_a \to \infty, \end{cases} \qquad D_a = 2a. \tag{111}$$

For finite N_a, the first half-height crossing connected to the central maximum defines

$$\begin{aligned}
\left|\frac{\widetilde{U}_{\mathrm{circ}}^{\mathrm{TH}}(v_{1/2}/(2\pi),0,1)}{\widetilde{U}_{\mathrm{circ}}^{\mathrm{TH}}(0,0,1)}\right|^2 = \frac{1}{2}, \qquad C_x(N_a) = \frac{2v_{1/2}}{\pi},\\
\mathrm{FWHM}_{x,f}^{\mathrm{circ,TH}} = C_x(N_a)\frac{\lambda f}{D_a}.
\end{aligned} \tag{112}$$

This defines C_x semianalytically: evaluate the complete slice profile, or a converged CHS representation, and solve one scalar half-height equation. Figure 5 shows its dependence on N_a. A simple estimate based on the arithmetic mean of the two asymptotic coefficients is

$$\mathrm{FWHM}_{x,f}^{\mathrm{circ,TH}} \simeq \overline{C}_x \frac{\lambda f}{D_a}, \qquad \overline{C}_x = \frac{1.02899397 + 0.88589294}{2} = 0.957443455. \tag{113}$$

It underestimates the Airy-like limiting width by 6.95% and overestimates the sinc-squared limiting width by 8.08%. These are endpoint deviations: the finite-N_a transition includes an undershoot, so they do not bound the error at every N_a. The complete-field root or circular moment formula below resolves that transition. All these transverse widths refer to $z = f$, independently of whether $z_p = f$.

The same stationary-phase reduction supplies a compact axial width near nominal focus. In Eq. 96, the non-focused integration selects the central chord $y' = 0$, while the focused quadratic coefficient becomes $\beta_x = -\mathrm{i}k(1/z - 1/f)/2$. The remaining factor is $S(\beta_x, 0; a)$, exactly the focused strip in Eqs. 60 and 81 with $a_x = a$ and zero Gaussian attenuation. Scaling $x' = as$ and normalizing by its zero-defocus value $2a$ gives

$$\psi_{\mathrm{TH}}(b) = \frac{1}{2}\int_{-1}^{1} e^{\mathrm{i}bs^2} ds = \frac{S(-\mathrm{i}b, 0; 1)}{2}, \qquad b = \frac{ka^2}{2}\left(\frac{1}{z} - \frac{1}{f}\right) = \pi N_a\left(\frac{f}{z} - 1\right), \qquad |\psi_{\mathrm{TH}}(b_{1/2})|^2 = \frac{1}{2}. \tag{114}$$

The even intensity has half-height roots $\pm b_{1/2}$, with $b_{1/2} = 2.7300019373\ldots$, half the $u_{1/2}$ in Eq. 65. Treating the non-focused multiplier and propagation prefactor as slowly varying, and linearizing $b \simeq -\pi N_a(z - f)/f$, gives $z_\pm \simeq f \pm f b_{1/2}/(\pi N_a)$ and

$$\mathrm{FWHM}_z^{\mathrm{circ,TH}} \simeq \frac{2\lambda f^2}{\pi a^2} b_{1/2} = 1.73797321\frac{\lambda f^2}{a^2}. \tag{115}$$

Its local half-extent is $\epsilon_z = b_{1/2}/(\pi N_a) = 0.8689866/N_a$; the strong-focus limit requires this to be small and the central-chord field reduction to be accurate. For the qualified circular top-hat references, the axial-width errors are 9.88%, 2.30% and 0.50% at $N_a = 5, 10, 100$, respectively. These examples quantify the approach to the limit without assigning one threshold to every Gaussian truncation. SI Section 6.4 gives the detailed transverse and axial derivations, finite-N_a root procedure and applicability evidence.

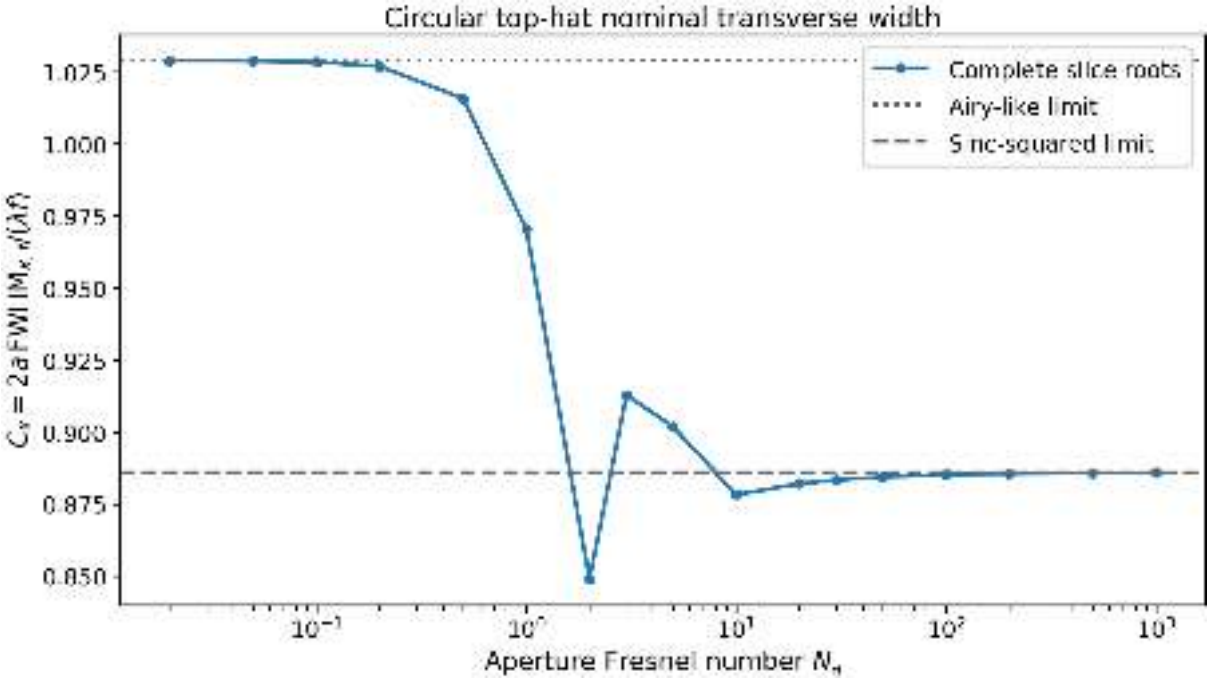


Figure 5: Circular top-hat nominal transverse-FWHM coefficient from complete finite-pupil slice roots, with the Airy-like and central-chord sinc-squared limits. Here $D_a = 2a$ and $\mathrm{FWHM}_{x,f} = C_x \lambda f / D_a$. The intermediate range is resolved by the complete circular slice field.

3.5.3 Untruncated Gaussian illumination: transverse and axial FWHMs

Expanding the stop to infinity at fixed w_L makes both Cartesian integration ranges infinite. Since $\mathrm{Re}\{\beta_x\} = \mathrm{Re}\{\beta_y\} = w_L^{-2} > 0$, each integral converges to $S(\beta, q; \infty) = \sqrt{\pi}\, e^{-q^2/(4\beta)}/\sqrt{\beta}$. Their product is

$$U_G(x,y,z) = \frac{C(x,y,z)A_0\pi}{\sqrt{\beta_x}\sqrt{\beta_y}} \exp\left[-\frac{(kx/z)^2}{4\beta_x} - \frac{(ky/z)^2}{4\beta_y}\right], \qquad w_x = w_y = w_L. \tag{116}$$

Dividing by the field at $x = 0$ and taking the squared modulus cancels the non-focused factor and observation phase. Solving the resulting Gaussian PSF at half height gives Eq. 68 with $w_x = w_L$, directly from the Gaussian integral. In particular,

$$\mathrm{FWHM}^G_{x,f} = \sqrt{2\ln 2}\,\frac{\lambda f}{\pi w_L}. \tag{117}$$

To expose the waist and axial intensity, write the propagated amplitude radii as

$$W_x^2(z) = w_L^2(1 - z/f)^2 + \left(\frac{\lambda z}{\pi w_L}\right)^2, \qquad W_y^2(z) = w_L^2 + \left(\frac{\lambda z}{\pi w_L}\right)^2. \tag{118}$$

With $s = \pi N_G = \pi w_L^2/(\lambda f)$, completing the square in W_x^2 gives $W_x^2 = w_{0G}^2[1 + ((z - z_{0G})/z_{RG})^2]$, where

$$\frac{z_{0G}}{f} = \frac{s^2}{1+s^2}, \qquad \frac{z_{RG}}{f} = \frac{s}{1+s^2}, \qquad w_{0G} = \frac{w_L}{\sqrt{1+s^2}}. \tag{119}$$

Here $z_{0G} = z_{t,G}$ is the minimum-thickness plane, not necessarily the intensity-peak plane. Setting $x = y = 0$ in Eq. 116 and retaining its propagation prefactor gives $I_G(z) \propto 1/[W_x(z)W_y(z)]$. Multiplying $W_x^2 W_y^2$ by the constant $s^4 f^4 / w_L^4$ therefore gives

$$I_G(z) \propto D_G(z)^{-1/2}, \qquad D_G(z) = [z^2 + s^2(f-z)^2][z^2 + s^2 f^2]. \tag{120}$$

The polynomial D_G makes the on-axis peak and half-height conditions algebraic. A peak is a positive minimum of D_G, selected with $D'_G(z_p) = 0$ and $D''_G(z_p) > 0$. The derivative equation is cubic. At half intensity,

$$\frac{I_G(z_\pm)}{I_G(z_p)} = \sqrt{\frac{D_G(z_p)}{D_G(z_\pm)}} = \frac{1}{2} \quad \Longrightarrow \quad D_G(z_\pm) = 4D_G(z_p), \qquad \mathrm{FWHM}_z^G = z_+ - z_-. \tag{121}$$

The quartic half-height equation uses the nearest positive crossings $z_- < z_p < z_+$ when both exist; they need not be symmetric. The factor four follows from squaring the intensity ratio, since I_G is proportional to $D_G^{-1/2}$. Substituting $z = f\tilde{z}$ and dividing D_G by f^4 gives the scaled polynomial in SI Section 6.4, equivalent to the general Gaussian cubic/quartic construction in SI Section 5.2.

When $s \gg 1$, W_y varies slowly across the focused waist. The axial intensity is then approximately proportional to $1/W_x$, so Eq. 70 gives half-height planes $z_{t,G} \pm \sqrt{3} z_{RG}$. Thus

$$\mathrm{FWHM}_{x,f}^G = \sqrt{2\ln 2}\frac{\lambda f}{\pi w_L}, \qquad \mathrm{FWHM}_z^G \simeq 2\sqrt{3}\, z_{RG} \simeq \frac{2\sqrt{3}\lambda f^2}{\pi w_L^2}. \tag{122}$$

The nominal transverse width is exact within the Gaussian Fresnel model. The last axial expression additionally uses $z_{RG} \simeq f/(\pi N_G)$ and requires the stated strong-focus conditions.

3.5.4 Truncated Gaussian illumination: profiles and FWHM roots

For finite τ, Eqs. 95 and 96 retain both finite integration limits. At nominal focus, the transverse half-height equation uses Eq. 95 with $\beta_x = w_L^{-2}$ and $\beta_y = w_L^{-2} - \mathrm{i}k/(2f)$. In the large-Fresnel central-chord limit, a simpler error-function profile is

$$\mathrm{PSF}_x(x \mid 0, f) \simeq \left|\frac{S(w_L^{-2}, kx/f; a)}{S(w_L^{-2}, 0; a)}\right|^2, \qquad \mathrm{FWHM}_{x,f} \simeq 2x_{1/2}, \quad \left|\frac{S(w_L^{-2}, kx_{1/2}/f; a)}{S(w_L^{-2}, 0; a)}\right|^2 = \frac{1}{2}. \tag{123}$$

Equation 94 evaluates this reduced profile without spatial quadrature; only its scalar half-height root remains numerical. For general N_a, use the complete circular field instead. SI Section 6.4 gives both the central-chord reduction and the small-N_a Gaussian-weighted Bessel profile.

The complete axial intensity follows by taking the squared modulus of Eq. 96. Its selected peak and neighboring half-height crossings determine the finite-pupil axial width, using the root construction of Section 3.4.1 and the broad-profile convention of Section 2.3.

Axial profile and half-height root. Near strong focus, the non-focused stationary-phase integration selects the chord at $y' = 0$, with endpoints $x' = \pm a$. Its remaining focused factor retains both Gaussian attenuation and the quadratic defocus phase. Substituting $x' = as$ gives

$$S\left[w_L^{-2} - \frac{\mathrm{i}k}{2}\left(\frac{1}{z} - \frac{1}{f}\right), 0; a\right] = a\int_{-1}^{1} e^{-\tau^2 s^2} e^{\mathrm{i}bs^2} ds = aS(\tau^2 - \mathrm{i}b, 0; 1), \qquad b = \pi N_a(f/z - 1). \tag{124}$$

Dividing this focused factor by its zero-defocus value gives the same normalized strip field as Eq. 81, with $a_x = a$ and $\tau_x = \tau$:

$$\psi(b) = \frac{S(\tau^2 - \mathrm{i}b, 0; 1)}{S(\tau^2, 0; 1)}, \qquad \psi(0) = 1, \qquad |\psi(b_{1/2})|^2 = \frac{1}{2}. \tag{125}$$

Here ψ is a dimensionless complex field; its squared modulus is the intensity profile.

The error-function strip supplies its half-height root directly by a scalar solve. Converting that root to an axial width uses the strong-focus assumptions already stated; the moment approximation to the same root follows in Section 3.5.5.

3.5.5 Moment-based FWHM formulas -- all regimes

Gaussian truncation enters these coefficients continuously. The transverse construction retains the complete circular pupil at the stated plane, while the compact axial construction uses the strong-focus central-chord profile of Section 3.5.4.

Complete circular transverse moments. Apply Section 3.3 to the complete circular Fresnel field in Eq. 95, with $a_0 = a$. Recall $s = x'/a$, $t = y'/a$ and $s^2 + t^2 \le 1$. Its quadratic weight is $e^{-B_x(z)s^2 - B_y(z)t^2}$, where $B_x = a^2\beta_x = \tau^2 - \mathrm{i}\pi N_a(\tilde{z}^{-1} - 1)$ and $B_y = \tau^2 - \mathrm{i}\pi N_a/\tilde{z}$. The common moments are therefore

$$M_{2j}(z) = \int_{-1}^{1} e^{-B_y(z)t^2} \left[\int_{-\sqrt{1-t^2}}^{\sqrt{1-t^2}} s^{2j} e^{-B_x(z)s^2} ds \right] dt, \qquad \mu_{2j}(z) = \frac{M_{2j}(z)}{M_0(z)}. \tag{126}$$

At nominal focus, $B_x = \tau^2$ and $B_y = \tau^2 - \mathrm{i}\pi N_a$. Using the real inner moments J_{2j} defined in Eq. 76 gives

$$\begin{aligned} M_{2j}(f) &= \int_{-1}^{1} e^{-(\tau^2 - \mathrm{i}\pi N_a)t^2} J_{2j}\left(\tau, \sqrt{1-t^2}\right) dt, \\ J_{2j}(\tau, h) &= \int_{-h}^{h} s^{2j} e^{-\tau^2 s^2} ds, \qquad j = 0, 1, 2, \ldots . \end{aligned} \tag{127}$$

The outer Fresnel phase and variable chord remain, so the complete circular moments are generally complex even at $z = f$. Their evaluation can use this quadrature or an analytical coefficient series. To obtain the series at any plane, expand only $e^{-B_x s^2}$ in Eq. 126. Each inner power integrates to

$$\int_{-h}^{h} s^{2j} e^{-B_x s^2} ds = 2 \sum_{n=0}^{\infty} \frac{(-B_x)^n h^{2(n+j)+1}}{n!\,[2(n+j)+1]}. \tag{128}$$

Setting $h^2 = 1 - t^2$ leaves an outer integral proportional to $\int_0^1 e^{-B_y u} u^{-1/2} (1-u)^{n+j+1/2} du$, after the substitution $u = t^2$. Its beta-integral representation is Kummer's confluent hypergeometric function ${}_1F_1$, giving [22]

$$M_{2j}(z) = \sqrt{\pi} \sum_{n=0}^{\infty} \frac{[-B_x(z)]^n}{n!} \frac{\Gamma(n+j+\frac{1}{2})}{\Gamma(n+j+2)} {}_1F_1\left(\tfrac{1}{2}; n+j+2; -B_y(z)\right). \tag{129}$$

At nominal focus, insert $B_x = \tau^2$, $B_y = \tau^2 - \mathrm{i}\pi N_a$ and set $j = 0, 1, 2$. The three coefficients needed for the fourth-order transverse width are explicitly

$$\begin{aligned} M_0(f) &= \sqrt{\pi} \sum_{n=0}^{\infty} \frac{(-\tau^2)^n \Gamma(n+\frac{1}{2})}{n!\,\Gamma(n+2)} {}_1F_1\left(\tfrac{1}{2}; n+2; -\tau^2 + \mathrm{i}\pi N_a\right), \\ M_2(f) &= \sqrt{\pi} \sum_{n=0}^{\infty} \frac{(-\tau^2)^n \Gamma(n+\frac{3}{2})}{n!\,\Gamma(n+3)} {}_1F_1\left(\tfrac{1}{2}; n+3; -\tau^2 + \mathrm{i}\pi N_a\right), \\ M_4(f) &= \sqrt{\pi} \sum_{n=0}^{\infty} \frac{(-\tau^2)^n \Gamma(n+\frac{5}{2})}{n!\,\Gamma(n+4)} {}_1F_1\left(\tfrac{1}{2}; n+4; -\tau^2 + \mathrm{i}\pi N_a\right). \end{aligned} \tag{130}$$

These are the same moment integrals as Eq. 127, now expressed without a remaining pupil quadrature. The sums retain finite Gaussian truncation and finite N_a. For a top-hat field at nominal focus, $B_x = 0$, so every term with $n > 0$ vanishes. Away from focus, top-hat defocus generally makes $B_x \neq 0$, and Eq. 129 retains that dependence. This coefficient evaluation is the moment counterpart of the CHS field representation in Section 4.3; SI Section 6.2 supplies the full integration steps and evaluation guidance.

Expanding the transverse factor $e^{-\mathrm{i}vs}$ in the complete circular field gives the normalized profile in Eq. 43. Its fourth-order natural-log intensity yields

$$\mathrm{FWHM}_{x,f} \simeq \frac{\lambda f}{\pi a} \left[\frac{2\ln 2}{A + \sqrt{A^2 + 4B\ln 2}} \right]^{1/2}. \tag{131}$$

Here the explicit coefficient construction is

$$\begin{aligned}
\mu_2 &= \frac{M_2}{M_0}, \qquad \mu_4 = \frac{M_4}{M_0}, \\
A &= \mathrm{Re}\{\mu_2\} = \mathrm{Re}\left\{\frac{M_2}{M_0}\right\}, \\
B &= \frac{\mathrm{Re}\{3\mu_2^2 - \mu_4\}}{12} = \frac{1}{12}\,\mathrm{Re}\left\{3\left(\frac{M_2}{M_0}\right)^2 - \frac{M_4}{M_0}\right\}.
\end{aligned} \tag{132}$$

The M_{2j} are evaluated at the same plane; the nominal formula uses $z = f$. For a nominal-plane top-hat field, the single surviving term gives

$$\mu_2 = \frac{{}_1F_1(\frac{1}{2}; 3; \mathrm{i}\pi N_a)}{4\,{}_1F_1(\frac{1}{2}; 2; \mathrm{i}\pi N_a)}, \qquad \mu_4 = \frac{{}_1F_1(\frac{1}{2}; 4; \mathrm{i}\pi N_a)}{8\,{}_1F_1(\frac{1}{2}; 2; \mathrm{i}\pi N_a)}. \tag{133}$$

Writing $F_j(N_a) = {}_1F_1(\frac{1}{2}; j; \mathrm{i}\pi N_a)$ for $j = 2, 3, 4$, substitution makes the finite-N_a top-hat coefficients themselves explicit:

$$A_{\mathrm{TH}}(N_a) = \frac{1}{4}\,\mathrm{Re}\left\{\frac{F_3}{F_2}\right\}, \qquad B_{\mathrm{TH}}(N_a) = \frac{1}{192}\,\mathrm{Re}\left\{3\left(\frac{F_3}{F_2}\right)^2 - 2\frac{F_4}{F_2}\right\}. \tag{134}$$

These depend on N_a even though the illumination is uniform. Their limits, together with the untruncated-Gaussian nominal-plane values, are

limit at $z = f$	μ_2	μ_4	A	B
circular top-hat, $N_a \to 0$	$1/4$	$1/8$	$1/4$	$1/192$
circular top-hat, $N_a \to \infty$	$1/3$	$1/5$	$1/3$	$1/90$
untruncated Gaussian	$1/(2\tau^2)$	$3/(4\tau^4)$	$1/(2\tau^2)$	0

(135)

The Gaussian row describes the ineffective-stop limit, not top-hat illumination. At any plane its moments are $\mu_2 = 1/[2a^2\beta_x(z)]$ and $\mu_4 = 3/[4a^4\beta_x(z)^2]$, so $B = 0$ and the transverse log-intensity formula is exact. For finite pupils, the branch and local-accuracy conditions of Section 3.3 apply. Against complete circular-profile half-height roots, Eq. 131 has a maximum sampled error of 0.482% for 1,254 cases: $0.03 \le N_a \le 200$ with $N_a = 1000$ also tested, and $0 \le \tau \le 3$ with $\tau = 4, 6$ also tested. SI Section 12.3 records this validation separately from coefficient convergence and arbitrary-plane accuracy.

Large-N_a central-chord moment approximation. A simpler coefficient evaluation follows by expanding the reduced profile of Eq. 123, rather than the complete circular field. Scaling $x' = as$ gives $S(w_L^{-2}, kx/f; a) = aS(\tau^2, v; 1)$. On normalization,

$$\begin{aligned}
\phi_{\mathrm{strip}}(v) &= \frac{S(\tau^2, v; 1)}{S(\tau^2, 0; 1)} = \frac{\int_{-1}^{1} e^{-\tau^2 s^2} e^{-\mathrm{i}vs}\, ds}{J_0(\tau, 1)} \\
&= 1 - \frac{\mu_2^{\mathrm{strip}} v^2}{2} + \frac{\mu_4^{\mathrm{strip}} v^4}{24} + O(v^6), \qquad \mu_{2j}^{\mathrm{strip}} = \frac{J_{2j}(\tau, 1)}{J_0(\tau, 1)}.
\end{aligned} \tag{136}$$

The coefficients are real because their nominal-plane weight $e^{-\tau^2 s^2}$ is real and positive. They are the explicit incomplete-gamma or error-function coefficients in Eqs. 76–77. Their log-intensity coefficients are $A = \mu_2^{\mathrm{strip}}$ and $B = [3(\mu_2^{\mathrm{strip}})^2 - \mu_4^{\mathrm{strip}}]/12$, inserted into the form of Eq. 131. This is the rectangular focused-strip approximation applied to the circular central-chord limit.

At fixed τ, stationary phase makes the normalized complete circular moments approach these strip moments as $N_a \to \infty$. At finite N_a, using them adds a geometry-reduction error. The numerical root of Eq. 123 and its fourth-order moment approximation must therefore be distinguished from the complete circular-field root and Eq. 131 with complete circular coefficients. On 144 matched saved pairs spanning $0 \le \tau \le 3$ and $10 \le N_a \le 1000$, their maximum width errors against complete circular roots are 0.881% and 1.295%, respectively. The separate 0.482% result above concerns complete circular moments on its stated sample. SI Section 6.4 details the central-chord expansion and these comparisons.

Axial moment width in the strong-focus regime. Expanding the axial phase $e^{\mathrm{i}bs^2}$ in the strip profile of Eq. 125 generates the real amplitude moments of s^2, rather than the transverse powers of s generated by $e^{-\mathrm{i}vs}$. With the strip moments in Eq. 136,

$$\psi(b) = 1 + \mathrm{i}\mu_2 b - \frac{\mu_4 b^2}{2} - \frac{\mathrm{i}\mu_6 b^3}{6} + \frac{\mu_8 b^4}{24} + O(b^5). \tag{137}$$

The variance V and fourth cumulant of s^2 are those in Eq. 83. Equations 84 and 86 give $|\psi|^{-4} = 1 + 2Vb^2 + Cb^4 + O(b^6)$ and its explicit limiting coefficients. At PSF half height, $|\psi|^2 = 1/2$ implies $|\psi|^{-4} = 4$. Solving $Cb_{1/2}^4 + 2Vb_{1/2}^2 - 3 = 0$ and using the local inverse-defocus conversion of Eq. 87 yields

$$\mathrm{FWHM}_z^{\mathrm{circ}} \simeq \frac{2\lambda f^2}{\pi a^2}\left[\frac{3}{V + \sqrt{V^2 + 3C}}\right]^{1/2}. \tag{138}$$

The coefficients in this axial expression follow from the real strip moments, rather than the complete complex circular moments above. For $\tau > 0$, define

$$T = \tau^2, \qquad E(\tau) = \frac{e^{-\tau^2}}{\sqrt{\pi}\tau\,\mathrm{erf}(\tau)}. \tag{139}$$

Insert the recurrence in Eq. 85 into $V = \mu_4 - \mu_2^2$ and $C = 2V^2 - \kappa_4/6$. This gives

$$\begin{aligned} V &= \frac{1}{2T^2} - E\left(1 + \frac{1}{2T}\right) - E^2, \\ C &= 3E^4 + \left(6 + \frac{3}{T}\right)E^3 + \left(\frac{19}{6} + \frac{19}{6T} - \frac{7}{8T^2}\right)E^2 \\ &\quad + \left(\frac{1}{6} + \frac{1}{4T} - \frac{13}{8T^2} - \frac{11}{16T^3}\right)E. \end{aligned} \tag{140}$$

These coefficients are explicit functions of Gaussian truncation and require only the error function and algebra. Their top-hat and untruncated-Gaussian limiting pairs are $(V, C) = (4/45, 16/945)$ and $(1/(2\tau^4), 0)$, respectively, as in Eq. 86. Near $\tau = 0$, the inverse-power terms cancel; the stable moment-series evaluation and the value at zero are given in SI Section 4.5.2. The coefficients apply to the circular axial width through the stated strong-focus central-chord reduction, and to the rectangular focused strip with $a = a_x$, $\tau = \tau_x$.

The calibrated $b_{1/2}^{\mathrm{cal}}$ in Eq. 89 also applies to this circular central-chord profile: it is the same reduced Gaussian-amplitude strip, followed by the same conversion $\mathrm{FWHM}_z \simeq 2\lambda f^2 b_{1/2}^{\mathrm{cal}}/(\pi a^2)$. Its 0.768% sampled strip-root error does not include the circular field-reduction error.

For transverse widths, rectangular and circular geometry enter different complete moment coefficients. For these reduced axial widths, the coefficients coincide because both calculations use the same focused-strip approximation; the complete axial fields remain different. The circular variable boundary, non-focused multiplier and propagation prefactor are retained by Eq. 96, which supplies the peak and connected half-height roots outside the qualified strong-focus range. SI Section 4.5.4 separates the strip-root approximation, field reduction and inverse-defocus conversion errors.

The moment-based FWHM relations retain truncation continuously and require no change of expression at $\tau = 0.75$ or 1.5. Complete nominal-plane circular moments retain N_a; compact axial expressions additionally require a valid strong-focus reduction. In the weakly truncated regime this depends on $N_G = N_a/\tau^2$, so increasing τ at fixed N_a can weaken Gaussian focusing. Finite-order top-hat moment widths remain approximations, whereas the Gaussian transverse log-intensity is exactly quadratic.

3.6 Scope and quadratic-phase generalizations

The common CASD formulation in Section 3.2 extends the analytical pupil-coordinate integration to optical elements whose pupil-plane phase contains constant, linear and quadratic terms. For Gaussian illumination, including its uniform top-hat limit, combining these terms with the Fresnel propagation phase preserves a quadratic–linear exponent along each transmitting interval. The same error-function strip evaluation therefore applies to rotated or combined lens powers, tilt and decentration within the scalar paraxial model.

CASD separates the pupil geometry from analytical evaluation of each interval. An x'-simple pupil has at most one connected transmitting interval $[x_-(y'), x_+(y')]$ per slice; more general finite unions use Eq. 34. The endpoints need not be symmetric, and sharp edges or gaps enter through their piecewise boundary functions. The inner integral is the integration over x': for a centered interval it is the strip function S of Eq. 29. Polynomial factors multiplying a Gaussian amplitude can also be integrated through the strip moments of Section 3.3.

Write the pupil-position vector, linear-phase vector and symmetric quadratic-phase matrix as

$$\mathbf{r}' = (x', y')^{\mathsf{T}}, \qquad \mathbf{l} = (l_x, l_y)^{\mathsf{T}}, \qquad \mathbf{Q} = \begin{pmatrix} Q_{xx} & Q_{xy} \\ Q_{xy} & Q_{yy} \end{pmatrix}. \tag{141}$$

Here T denotes ordinary transpose, so the row–column and row–matrix–column products below are scalars. The constant ϕ_0 is an overall pupil phase, $\mathbf{l}$ contains tilt or decentration-induced linear phase, and $\mathbf{Q}$ describes the total quadratic phase of the pupil-plane optical elements, including the cylindrical lens:

$$\begin{aligned} \Phi_{\mathrm{tot}}(x', y') &= \phi_0 + \mathbf{l}^{\mathsf{T}}\mathbf{r}' + \frac{1}{2}\mathbf{r}'^{\mathsf{T}}\mathbf{Q}\mathbf{r}' \\ &= \phi_0 + l_x x' + l_y y' + \frac{1}{2}\left[Q_{xx}x'^2 + 2Q_{xy}x'y' + Q_{yy}y'^2\right]. \end{aligned} \tag{142}$$

For the original lens with an additional pupil phase, $\Phi_{\mathrm{tot}} = -kx'^2/(2f) + \Phi_{\mathrm{add}}$. Substituting this total phase into the Fresnel field includes the lens once; free-space propagation adds $k\mathbf{I}/z$ to the quadratic-phase matrix, with $\mathbf{I}$ the identity matrix. For the Gaussian amplitude of Section 2.2, collecting powers of x' and y' gives

$$\begin{aligned} \hat{\beta}_x &= \frac{1}{w_x^2} - \frac{\mathrm{i}}{2}\left(Q_{xx} + \frac{k}{z}\right), \qquad \hat{\beta}_y = \frac{1}{w_y^2} - \frac{\mathrm{i}}{2}\left(Q_{yy} + \frac{k}{z}\right), \\ \hat{q}_x(y') &= q_x - l_x - Q_{xy}y', \qquad q_x = \frac{kx}{z}, \quad q_y = \frac{ky}{z}. \end{aligned} \tag{143}$$

At fixed y', $Q_{xy}y'$ is a known coefficient multiplying x'. It changes the strip's linear-phase argument from q_x to $\hat{q}_x(y')$, while the exponent remains quadratic–linear in x'. Consequently,

$$\int_{-L(y')}^{L(y')} e^{-\widehat{\beta}_x x'^2 - \mathrm{i}\hat{q}_x(y')x'}\,dx' = S\big(\hat{\beta}_x, \hat{q}_x(y'); L(y')\big), \tag{144}$$

and the centered single-interval field becomes

$$U_{\mathcal{D}}(x, y, z) = CA_0 e^{\mathrm{i}\phi_0} \int_y e^{-\widehat{\beta}_y y'^2 - \mathrm{i}(q_y - l_y)y'} S\big(\hat{\beta}_x, \hat{q}_x(y'); L(y')\big)\,dy', \tag{145}$$

with C from Eq. 22. This is the same analytical strip evaluation followed by one outer quadrature. Uniform top-hat illumination sets $w_x^{-2} = w_y^{-2} = 0$; the continuous strip branch of Section 3.2 applies if a resulting quadratic coefficient vanishes.

A rotated cylindrical lens, for example, has

$$\Phi_{\mathrm{rot}} = -\frac{k}{2f}(x'\cos(\vartheta) + y'\sin(\vartheta))^2, \tag{146}$$

whereas combined cylindrical and spherical powers give

$$\Phi_{c+s} = -\frac{k}{2}\left[(f_c^{-1} + f_s^{-1})x'^2 + f_s^{-1}y'^2\right]. \tag{147}$$

Crossed cylindrical lenses and toroidal powers belong to the same class. The circular and elliptical chords in Eq. 27 retain one outer quadrature. For the rectangular pupil, $L = a_x$ is constant: the field separates into two analytical strips when $Q_{xy} = 0$, whereas a cross-phase term leaves a coupled outer quadrature. General

transmitting intervals use the same error-function antiderivative at their endpoints and sum the complex contributions. SI Section 7.2 gives that interval-sum field and includes a mixed Gaussian-amplitude term.

The extension supplies fields for these optical elements and pupil geometries; the FWHM comparisons remain those established for the rectangular and circular configurations studied here. SI Section 7.3 gives further examples and the scope of the numerical check. Some phases of higher total degree also preserve the analytical strip when they remain at most quadratic in the eliminated coordinate; the coordinate choice and finite-interval moment-series route for other polynomial phases are discussed in SI Section 7.4.

3.7 Connections with comparable cylindrical and established focal-field frameworks

The rectangular field provides the closest invariant-axis cylindrical baseline [6]. For the circular pupil of physical radius a, introduce the dimensionless radial coordinate $\rho = r'/a$ and polar angle θ:

$$x' = a\rho\cos(\theta), \qquad y' = a\rho\sin(\theta), \qquad dx'\,dy' = a^2\rho\,d\rho\,d\theta, \qquad 0 \le \rho \le 1, \quad 0 \le \theta < 2\pi. \tag{148}$$

Let $q = (q_x^2 + q_y^2)^{1/2}$ and $\varphi = \operatorname{atan2}(q_y, q_x)$, where atan2 is the quadrant-resolving polar angle of the ordered pair (q_x, q_y). The complete pupil-dependent part of the Fresnel field is then

$$K(q,\varphi,z) = a^2 \int_0^1 \rho e^{-\tau^2\rho^2} \int_0^{2\pi} \exp[\mathrm{i}\alpha\rho^2 + \mathrm{i}\gamma\rho^2\cos(2\theta)] \times \exp[-\mathrm{i}qa\rho\cos(\theta-\varphi)]\,d\theta\,d\rho, \tag{149}$$

with

$$\alpha = \pi N_a\left(\tilde{z}^{-1} - \frac{1}{2}\right), \qquad \gamma = -\frac{\pi N_a}{2}. \tag{150}$$

Equivalently, the Gaussian-weighted quadratic pupil factor before the last Fourier kernel is

$$\exp(-\tau^2\rho^2)\exp\left\{\mathrm{i}\pi N_a\rho^2\left[\left(\tilde{z}^{-1} - \frac{1}{2}\right) - \frac{1}{2}\cos(2\theta)\right]\right\}. \tag{151}$$

Thus the circular cylindrical-lens phase is rotationally symmetric defocus ($\alpha\rho^2$) plus primary astigmatism ($\gamma\rho^2\cos(2\theta)$). A top-hat has unit radial amplitude, whereas a Gaussian contributes $e^{-\tau^2\rho^2}$ and changes the radial Zernike coefficients. Expanding the complete plane-dependent pupil factor in Zernike modes and applying their analytical Fourier transforms gives an independent scalar reconstruction. The implemented expansion agrees with the slice field to below 1.5×10^{-9} at three selected top-hat/truncated-Gaussian checks with $N_a \le 3$. In the ENZ through-focus construction, defocus is instead retained in the radial basis functions while the pupil coefficients remain fixed [16]. SI Section 8 distinguishes these two calculations and displays the cylindrical specialization.

The cited frameworks address complementary parts of the problem. Li and Wolf quantify finite-Fresnel deformation and focal displacement for circular focal fields [9]; Sheppard analyzes finite-Fresnel imaging with hard circular and Gaussian pupils [10]; Mahajan, Li and Yu, Urey, and Dupraz *et al.* treat Gaussian apodization, truncation, axial irradiance, or moment expansions [11–15]. Sheppard's 2015 line-wise transforms describe isotropic point focusing through two-dimensional pupils [8]. ENZ accommodates general circular-pupil aberrations and extends naturally to vector high-aperture fields [17]. For the present scalar cylindrical problem, however, ENZ does not turn the transverse or axial FWHM into simpler universal closed roots: a basis projection and convergence choice precede the same numerical half-maximum operation. The Cartesian slice form is therefore the direct evaluator for the four stated pupil–illumination families, while ENZ supplies an independent analytical reconstruction and an extension route. SI Section 8 develops the Zernike/ENZ equations and vector extension.

Urey's fitted relations describe circularly truncated, rotationally focused Gaussian spots and depth of focus at specified Strehl levels [14]. Their axial criterion is referenced to nominal focal irradiance, whereas the present FWHM_z is referenced to the selected axial peak. Dupraz *et al.* use a moment expansion to evaluate circular-aperture diffraction of Gaussian and Laguerre–Gauss beams [15]. Here the moments are taken from the cylindrical focal slice, including its orthogonal Fresnel phase, and used to solve a fourth-order log-intensity approximation for FWHM. Once these moments have been evaluated, the explicit width follows without a spatial half-maximum root search.

4 Special planes, analytical series and reductions

4.1 Nominal focal plane and axial propagation planes

At the nominal focal plane $z = f$, $\beta_x = 1/w_L^2$ and $\beta_y = 1/w_L^2 - \mathrm{i}k/(2f)$. For a top-hat, the focused-coordinate quadratic phase vanishes, whereas the non-focused coordinate retains its Fresnel phase. The rectangular focal profile is Eq. 63, and the circular focal profile is Eq. 103. A circular top-hat therefore need not have either the Airy profile of an isotropic spherical focus or the exact sinc profile of a fixed-width slit. At $y = 0$, the remaining circular-slice integrand is even in y' and may be evaluated over $0 \le y' \le a$ with a factor of two. Figure 6 shows the normalized intensities $|U|^2$, not field amplitudes.

The square top-hat row is evaluated from Eq. 57, the two stopped circular rows from Eq. 100, and the untruncated-Gaussian row from Eq. 116. The left column is the transverse xy plane at $z = f$; the right is the central xz plane at $y = 0$. One intensity normalization is shared between both panels of each row. The fine y-directed fringes in the square top-hat focal map are physical Fresnel diffraction from the finite non-focused hard edges: Eq. 57 evaluates them analytically. For scale, $\lambda = 633$ nm, $a = 5$ mm, and $f = 400$ mm give $N_a = 98.736$, one transverse unit equal to 50.64 μm, and one axial unit equal to 400 mm. SI Section 9 gives linear/logarithmic panels and recalculated dimensional maps for precisely these physical values, together with equal-scale and thickness-magnified views.

Finite Fresnel number requires several distinct axial planes: the geometrical focal plane $z = f$, the principal on-axis intensity maximum $z = z_p$, the minimum-thickness plane $z = z_t$ within the principal focal support, and, in the Gaussian limit, the focused waist plane. They need not coincide. The xz axial-propagation plane has $y = 0$ with x and z varying; it is not an additional focal-plane approximation.

4.2 Optical axis and incomplete-gamma series

On the optical axis, $q_x = q_y = 0$. In polar coordinates, the quadratic exponent is

$$-\beta_x r^2 \cos^2(\theta) - \beta_y r^2 \sin^2(\theta) = -pr^2 - dr^2 \cos(2\theta), \tag{152}$$

where

$$p = \frac{\beta_x + \beta_y}{2}, \qquad d = \frac{\beta_x - \beta_y}{2}. \tag{153}$$

The physical on-axis field is $U_{\mathrm{ax}}(z) = U(0, 0, z) = C_{\mathrm{ax}} A_0 K_{\mathrm{ax}}(z)$. Using $\int_0^{2\pi} e^{-dr^2 \cos(2\theta)} d\theta = 2\pi I_0(dr^2)$ and then $t = r^2$, so $r\,dr = dt/2$, gives

$$K_{\mathrm{ax}}(z) = \pi \int_0^{a^2} e^{-pt} I_0(dt) dt. \tag{154}$$

Here I_0 is the modified Bessel function of the first kind of order zero and t is the squared physical pupil radius. Expanding $I_0(dt) = \sum_{m=0}^{\infty} (dt/2)^{2m}/(m!)^2$ and integrating each power of t gives the exact incomplete-gamma series

$$K_{\mathrm{ax}}(z) = \pi \sum_{m=0}^{\infty} \frac{d^{2m}}{4^m (m!)^2} \frac{\gamma(2m+1, pa^2)}{p^{2m+1}}. \tag{155}$$

where the lower incomplete gamma function is

$$\gamma(s, x) = \int_0^x v^{s-1} e^{-v} dv. \tag{156}$$

Although $\gamma(2m+1, pa^2)/p^{2m+1}$ appears singular at $p = 0$, the limit is finite because it equals the defining integral $\int_0^{a^2} t^{2m} e^{-pt} dt \to a^{4m+2}/(2m+1)$. This branch includes, for example, the top-hat case at $z = 2f$. The series supplies an independent on-axis field from which z_p and the two connected half-maximum roots defining FWHM_z can be calculated. At large N_a, direct evaluation requires sufficiently high order and precision;

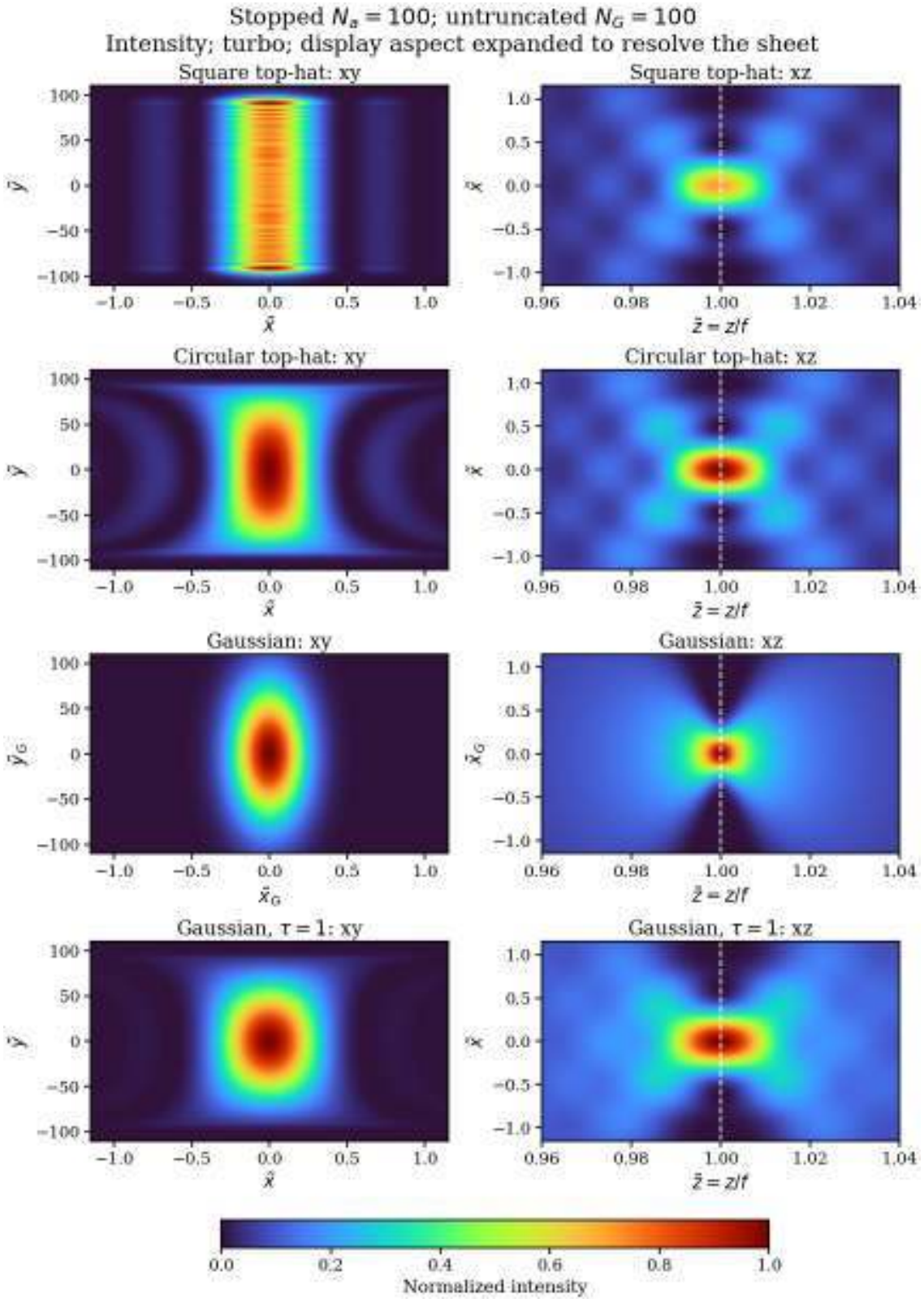


Figure 6: Nominal transverse and central axial intensity for square top-hat, circular top-hat, circular untruncated Gaussian, and circular Gaussian truncated at $\tau = 1$. Stopped cases use $N_a = 100$ and the untruncated case uses $N_G = 100$. Transverse coordinates are $\tilde{x} = ax/(\lambda f)$ and $\tilde{y} = ay/(\lambda f)$ for stopped pupils, with a replaced by w_L for the untruncated Gaussian. Every axial panel uses $\tilde{z} = z/f$; the dashed line marks 1. The display aspect is expanded to resolve the sheet thickness and does not represent equal physical lengths. Maps use turbo.

the exact polar or slice quadrature remains the production route. SI Section 9.2 gives the derivation and convergence details.

4.3 Specialized full focal-region series

Polar Bessel–incomplete-gamma (PBIG) series. The circular field in Eq. 92 can first be organized by angular harmonics. Put $x' = r\cos(\theta)$, $y' = r\sin(\theta)$, with dimensional radius $0 \le r \le a$ and area element $dx'\,dy' = r\,dr\,d\theta$. Thus $r = a\rho$ in the normalized polar coordinates of Eq. 149. For an arbitrary observation point, let $q = (q_x^2 + q_y^2)^{1/2}$ and $\varphi = \mathrm{atan2}(q_y, q_x)$. The two-argument function $\mathrm{atan2}(q_y, q_x)$ returns the polar angle in the correct quadrant; when $q = 0$, the result is independent of this angle. With the coefficients $p = (\beta_x + \beta_y)/2$ and $d = (\beta_x - \beta_y)/2$ already used on axis,

$$\begin{aligned} \beta_x x'^2 + \beta_y y'^2 &= pr^2 + dr^2\cos(2\theta), \\ q_x x' + q_y y' &= qr\cos(\theta - \varphi). \end{aligned} \tag{157}$$

Substitution into the pupil integral therefore gives the complete field as $U_{\mathrm{circ}} = CA_0K$, where

$$K = \int_0^a re^{-pr^2} \int_0^{2\pi} e^{-dr^2\cos(2\theta)} e^{-\mathrm{i}qr\cos(\theta-\varphi)}\,d\theta\,dr. \tag{158}$$

The first angular factor has modified-Bessel coefficients $(-1)^m I_m(dr^2)$ at orders $2m$. The Jacobi–Anger expansion of the second factor has ordinary-Bessel coefficients $(-\mathrm{i})^n J_n(qr)$. Angular integration retains $n = \pm 2m$; the phase factors cancel and the paired harmonics combine into $\cos(2m\varphi)$. This gives

$$K = 2\pi\left[R_0 + 2\sum_{m=1}^{\infty} R_m\cos(2m\varphi)\right], \qquad R_m = \int_0^a re^{-pr^2} I_m(dr^2) J_{2m}(qr)dr, \tag{159}$$

Here R_m is the radial coefficient at even angular order $2m$. Expanding $I_m(dr^2)$ and $J_{2m}(qr)$ gives a double sum of radial powers, each integrated by

$$\int_0^a r^{2s+1}e^{-pr^2}dr = \frac{\gamma(s+1, pa^2)}{2p^{s+1}}, \qquad s = 0, 1, 2, \ldots. \tag{160}$$

At $p = 0$ the integral is $a^{2s+2}/[2(s+1)]$ by continuity. These coefficients give the PBIG series explicitly; direct numerical integration of R_m gives the equivalent direct-radial harmonic representation. When $q = 0$, $J_{2m}(0) = 0$ for $m > 0$, so only R_0 survives and the representation reduces to the axial form.

The full-region series reconstructs the complex field away from the optical axis and can therefore generate transverse profiles and their FWHM roots. Direct radial evaluation of each R_m separates angular truncation from the inner power-series truncation and cancellation in the closed double expansion. Individual expanded terms can greatly exceed the final field, so both radial order and arithmetic precision must be converged. The direct-radial harmonics provide a useful independent check through $N_a = 100$ on the declared stencil; the Cartesian slice remains the routine point evaluator. SI Section 9.3 gives the complete derivation, the separate truncation controls, and the order/error tables.

Cartesian hypergeometric series (CHS). An alternative organization follows directly from the aperture-slice field in Eq. 100. Its coefficients contain Kummer's confluent hypergeometric function, which retains the non-focused quadratic factor analytically. With pupil coordinates $u = x'/a$, $t = y'/a$, and $D = \{(u,t) : u^2 + t^2 \le 1\}$, define the dimensionless kernel

$$H = \iint_D e^{-B_x u^2 - B_y t^2 - \mathrm{i}Q_x u - \mathrm{i}Q_y t}\,du\,dt, \qquad U_{\mathrm{circ}} = CA_0a^2H. \tag{161}$$

Thus $K = a^2H$ in Eq. 159, and $\widetilde{U}_{\mathrm{circ}} = (N_a/\tilde{z})H$ in Eq. 100. The coefficients B_x, B_y, Q_x, Q_y retain Eqs. 98 and 99. The disk and its generally complex weight $W(u,t) = e^{-B_x u^2 - B_y t^2}$ are invariant under each reflection $u \mapsto -u$ and $t \mapsto -t$. In the product $(\cos(Q_x u) - \mathrm{i}\sin(Q_x u))(\cos(Q_y t) - \mathrm{i}\sin(Q_y t))$, every sine-containing term is odd in at least one coordinate. Its integral vanishes, including the sine–sine term, which is odd under either reflection separately. Consequently,

$$
\begin{aligned}
H &= \iint_D W(u,t)\cos(Q_x u)\cos(Q_y t)\,du\,dt \\
&= \int_{-1}^{1} e^{-B_y t^2}\cos(Q_y t) S\big(B_x, Q_x; \sqrt{1-t^2}\big)\,dt.
\end{aligned}
\tag{162}
$$

The remaining integral is complex and retains the circular chord coupling. This symmetry argument applies to the centered pupil and diagonal quadratic weight considered here. Expanding the focused factor and integrating its powers over a chord of half-width $h = \sqrt{1-t^2}$ gives

$$
\begin{aligned}
e^{-B_x u^2}\cos(Q_x u) &= \sum_{n=0}^{\infty} c_n u^{2n}, \qquad c_n = \sum_{j=0}^{n} \frac{(-B_x)^{n-j}(-1)^j Q_x^{2j}}{(n-j)!(2j)!}, \\
S(B_x, Q_x; h) &= 2\sum_{n=0}^{\infty} \frac{c_n h^{2n+1}}{2n+1}.
\end{aligned}
\tag{163}
$$

Expand $\cos(Q_y t)$ in the remaining integral, but retain $e^{-B_y t^2}$. The substitution $s = t^2$ converts each term into a beta-weighted exponential integral, evaluated by Kummer's confluent hypergeometric function ${}_1F_1$ [22]. The resulting full double sum is

$$
\begin{aligned}
H = \sum_{n=0}^{\infty}\sum_{r=0}^{\infty} &\frac{c_n(-1)^r Q_y^{2r}}{(2r)!}\frac{\Gamma(n+\frac{1}{2})\Gamma(r+\frac{1}{2})}{\Gamma(n+r+2)} \\
&\times {}_1F_1\big(r+\tfrac{1}{2}; n+r+2; -B_y\big).
\end{aligned}
\tag{164}
$$

All powers of B_y are included in ${}_1F_1$; this partial resummation leaves only the focused factor and non-focused linear phase expanded. Each term is evaluated without a spatial quadrature. The series is absolutely convergent for fixed finite coefficients on the bounded pupil. Its infinite sum therefore represents the full scalar Fresnel field for finite τ, N_a and $z > 0$, while a finite numerical sum requires convergence in both retained orders and arithmetic precision. In the entire xz axial-propagation plane $y = 0$, $Q_y = 0$ removes every $r > 0$ term:

$$
H(\tilde{x}, 0, \tilde{z}) = \sqrt{\pi}\sum_{n=0}^{\infty} c_n \frac{\Gamma(n+\frac{1}{2})}{\Gamma(n+2)}\,{}_1F_1\big(\tfrac{1}{2}; n+2; -B_y\big).
\tag{165}
$$

On the optical axis, $c_n = (-B_x)^n/n!$. For a circular top-hat at nominal focus, $B_x = 0$, so the on-axis field reduces to the single special-function expression

$$
H(0,0,1;\tau=0,N_a) = \pi\,{}_1F_1\big(\tfrac{1}{2}; 2; \mathrm{i}\pi N_a\big).
\tag{166}
$$

The CHS is particularly useful near nominal focus: the focused quadratic phase becomes small while the non-focused phase can remain large and is retained inside ${}_1F_1$. However, $B_x = \tau^2 - \mathrm{i}\pi N_a(\tilde{z}^{-1} - 1)$ still contains the Gaussian amplitude term. Large τ (weak truncation), appreciable defocus, or large off-axis coordinates can require many terms. PBIG instead resolves angular harmonics and then radial powers; its direct-radial version avoids the inner expansion at the cost of quadrature. These complementary organizations provide independent full-field evaluations, without imposing the strong-focus reduction used for compact axial widths.

The same CHS coefficients also supply the moments in Eq. 129. At fixed z and $y = 0$, write $v = Q_x$; expanding only the transverse Fourier factor gives

$$
H(v, 0; z) = \sum_{j=0}^{\infty} \frac{(-1)^j M_{2j}(z)}{(2j)!} v^{2j}, \qquad \phi(v; z) = \frac{H(v, 0; z)}{M_0(z)}.
\tag{167}
$$

The normalized intensity is $|\phi|^2$. A converged field supplies numerical half-height roots, while truncating its natural-log intensity supplies the explicit moment width in Eq. 131. At intermediate truncation $\tau = 1$, retaining four terms for each of M_0, M_2, M_4 gives a maximum sampled transverse-FWHM error of 0.866% over $N_a = 0.1, 1, 3, 10, 30, 100, 1000$. That error includes both the finite moment-coefficient truncation and the fourth-order log-intensity approximation; compact axial formulas introduce a further strong-focus reduction.

SI Section 9.4 gives the complete derivation, convergence argument and limiting cases; SI Section 4 gives the explicit moment series and its width errors. Numerical evaluation and the retained physical prefactor are assessed in Section 5.

Recurrence-based incomplete-gamma (RIG) series. A complementary organization retains the common radial Gaussian and quadratic-phase factor while grouping the remaining Cartesian powers by total degree. Using the dimensionless kernel H of Eq. 161, put

$$\tilde{p} = a^2 p = \frac{B_x + B_y}{2}, \qquad \tilde{d} = a^2 d = \frac{B_x - B_y}{2}, \qquad P = Q_x^2 + Q_y^2, \qquad T = Q_x^2 - Q_y^2. \tag{168}$$

The integrand then factors into $e^{-\tilde{p}(u^2+t^2)} e^{-\tilde{d}(u^2-t^2)-\mathrm{i}(Q_x u + Q_y t)}$. On writing $u = \rho\cos(\theta)$, $t = \rho\sin(\theta)$, the angular mean of the second factor is $\sum_{n\geq 0} g_n \rho^{2n}/n!$: reflection symmetry removes odd total powers. Each remaining radial power is integrated analytically, giving the full-field representation

$$H = \pi \sum_{n=0}^{\infty} \frac{g_n}{n!} V_n(\tilde{p}), \qquad V_n(\tilde{p}) = \frac{\gamma(n+1, \tilde{p})}{\tilde{p}^{n+1}}, \qquad V_n(0) = \frac{1}{n+1}. \tag{169}$$

Here $U_{\mathrm{circ}} = C A_0 a^2 H$ retains the same physical prefactor as CHS. The coefficients follow a finite recurrence,

$$\begin{aligned} (n+1) g_{n+1} = & -\frac{P}{4} g_n + \left[\tilde{d}^2 (2n-1) + \frac{\tilde{d} T}{2}\right] g_{n-1} \\ & - \frac{P \tilde{d}^2}{4} g_{n-2} - \tilde{d}^4 (n-2) g_{n-3}, \qquad n \geq 0, \end{aligned} \tag{170}$$

with $g_0 = 1$ and $g_n = 0$ for negative indices. For example, $g_1 = -P/4$ and $g_2 = P^2/32 + \tilde{d}^2/2 + \tilde{d}T/4$. Thus each term requires an analytical radial factor and previously computed coefficients. On axis, $g_{2m} = (2m)!\tilde{d}^{2m}/[4^m (m!)^2]$ and $g_{2m+1} = 0$; after restoring a^2, Eq. 169 reduces exactly to the axial incomplete-gamma series in Eq. 155.

RIG groups total-degree contributions to the same circular field represented by PBIG and CHS. It retains the common radial weight, whereas CHS retains the non-focused quadratic weight and PBIG resolves angular harmonics. All three are exact at infinite order for fixed finite parameters. Their finite sums have different truncation and cancellation costs: the retained radial weight can be useful for weak Gaussian truncation and defocus, while CHS is particularly compact near nominal focus. SI Section 9.5 derives the recurrence, continuous limits and convergence conditions; the matched numerical comparisons are in SI Section 10.3.1.

5 Numerical evaluation and validation

For Gauss–Legendre nodes t_j and weights w_j on the finite chord coordinate,

$$\int_{-1}^{1} g(t)dt \simeq \sum_{j=1}^{n_q} w_j g(t_j). \tag{171}$$

Gauss–Legendre quadrature places nodes and weights so that an n_q-node rule integrates polynomials through degree $2n_q - 1$ exactly. The circular chord produces square-root endpoint behavior in the original coordinate $t = y'/a$. The substitution $t = \sin(\theta)$, $dt = \cos(\theta)\, d\theta$, regularizes that endpoint behavior on $-\pi/2 \leq \theta \leq \pi/2$ and is used for the refined focal-width calculations. Both forms vectorize over observation points. Rapid quadratic phase at high N_z still requires repeated-order comparison: a fixed-order Gauss–Legendre rule has no intrinsic error estimate.

The circular field is evaluated by Gauss–Legendre quadrature of Eq. 100. A Faddeeva-function implementation of Eq. 31 avoids overflow and subtractive cancellation for large imaginary error-function arguments; the removable sinc branch is evaluated explicitly. Independent checks use direct two-dimensional polar quadrature, the polar on-axis integral, the rectangular closed field, Gaussian and sinc limits, and the analytical series. Transverse half-maximum roots are obtained from resolved profiles using shape-preserving interpolation; the

refined axial roots are evaluated directly by quadrature inside their brackets. Numerical work uses NumPy and SciPy [23, 24].

The representative relative complex-field discrepancy between circular slice and independent polar quadrature is 8.77×10^{-9}; the general ellipse/quadratic-phase implementation agrees with an independently assembled polar integral to 3.55×10^{-9}. Rectangular tests recover the sinc-squared limit to 6.66×10^{-16} and the untruncated-Gaussian defocused FWHM to 2.29×10^{-11}. The automated test suite also checks limiting branches, symmetry, factor cancellation, metric extraction, notation migration, plane-by-plane scalar Zernike reconstruction, direct-radial harmonics, exact-Snell limits, and data schemas. The circular-slice *order* is the number of Gauss–Legendre nodes retained in the remaining t integral. At $N_a = 1000$, increasing this order from 2400 to 4000 changes the selected nine-point top-hat stencil by at most 1.48×10^{-9} after global complex-field normalization; the 3200-to-4000 change is 3.88×10^{-10}.

The wide sheet-height maps impose a stronger quadrature requirement than the near-axis stencil. At $N_a = 1000$, the displayed yz maps use 8632 nodes after lower-order rules were found to under-resolve the phase near the sheet edges. Repeating the map checks at 1.5 times the production order, including the axis, edges, and points outside the stop projection, gives a largest sampled normalized intensity change of 1.33×10^{-12} over the stated top-hat and $\tau = 1$ map families. This repeated-order test concerns quadrature accuracy; the plotted pixel grid is a separate sampling choice.

For a declared validation stencil Ω, Figure 7 plots the globally normalized complex-field error

$$\epsilon_n = \frac{\max_\Omega |U_n - U_{\mathrm{ref}}|}{\max_\Omega |U_{\mathrm{ref}}|}. \tag{172}$$

Figure 7 compares four analytical representations for truncated-Gaussian illumination, $\tau = 1$, at $N_a = 0.1, 1, 10, 100$. The axial incomplete-gamma series is evaluated at $x = y = 0$ on five planes, $\tilde{z} = 0.5, 0.75, 1, 1.25, 1.5$. PBIG, CHS and RIG use the same 15-point xz stencil, adding $\tilde{x} = 0.15, 0.35$ at each plane while retaining $\tilde{y} = 0$; reflection symmetry supplies the negative-x counterparts. The comparison includes the propagation-amplitude factor $N_a/\tilde{z}$. These samples resolve differences between the series organizations without treating axial-only expressions as arbitrary-point fields. The SI adds $N_a = 30$, reference-refinement checks, the retained orders and the cost of reaching 0.1% sampled field error.

The horizontal order has a distinct meaning for each representation: axial term count; PBIG radial j count with $m_{\max} = 12$ and 24 Fourier-radial terms; CHS focused-coordinate term count, with one nonzero y-Fourier term; and RIG radial-degree term count. Independent order and precision increases test the accepted settings. Large intermediate terms can require substantially more precision than binary64, especially at high Fresnel number. An apparently smooth intensity map or small angular order alone does not establish convergence of the complete analytical sum.

The CHS, Eqs. 164 and 165, was checked separately on six truncations $\tau = 0, 0.5, 1, 1.5, 2, 3$, seven Fresnel numbers $N_a = 0.1, 1, 3, 10, 30, 100, 1000$, and nine spatial points per pair. Of 378 samples, 336 meet the declared 10^{-8} normalized complex-field tolerance after independent quadrature, order and precision checks; 42 lie outside the selected evaluation budget and are excluded from that accuracy statement. The maximum observed normalized discrepancy among accepted samples is 7.02×10^{-13}, with normalization and the complete stencil specified in SI Section 10. At $\tau = 1, N_a = 100, x = y = 0, z = f$, four, eight and twelve terms in Eq. 165 give relative field errors of 0.532%, 1.78×10^{-6} and 1.05×10^{-10}, respectively. These are pointwise convergence results, distinct from the four-term moment approximation above.

Using the same selected focal branch and validated reference brackets, the CHS reproduces 42 nominal-plane transverse widths, 35 peak-plane transverse widths and 35 connected axial widths within a relative tolerance of 10^{-5}. This check compares CHS and quadrature roots of the raw intensity in matched local brackets; it tests agreement of the field representations, separately from the broad-profile peak selection used for oscillatory practical-width comparisons in Section 2.3. Seven axial reference cases remain unvalidated within the bounded search. Axial roots use $(N_a/\tilde{z})^2|H|^2$, retaining the propagation prefactor. The evaluation uses arbitrary-precision complex ${}_1F_1$ values checked against their Euler integral; converged outer sums alone do not test the special-function backend. This representation is economical near focus relative to the compared power-series configurations, whereas vectorized slice quadrature remains the routine general field evaluator.

The RIG recurrence and its axial and isotropic limits are checked independently. Nine additional nonzero-y samples agree with refined polar and slice references to a largest relative field discrepancy of 3.72×10^{-14}. Additional matched Gaussian pointwise comparisons of CHS, analytical PBIG, RIG and degree-2 to degree-8 moment fields report both 10^{-10} and 0.1% relative field targets. It includes the cost of coefficients and

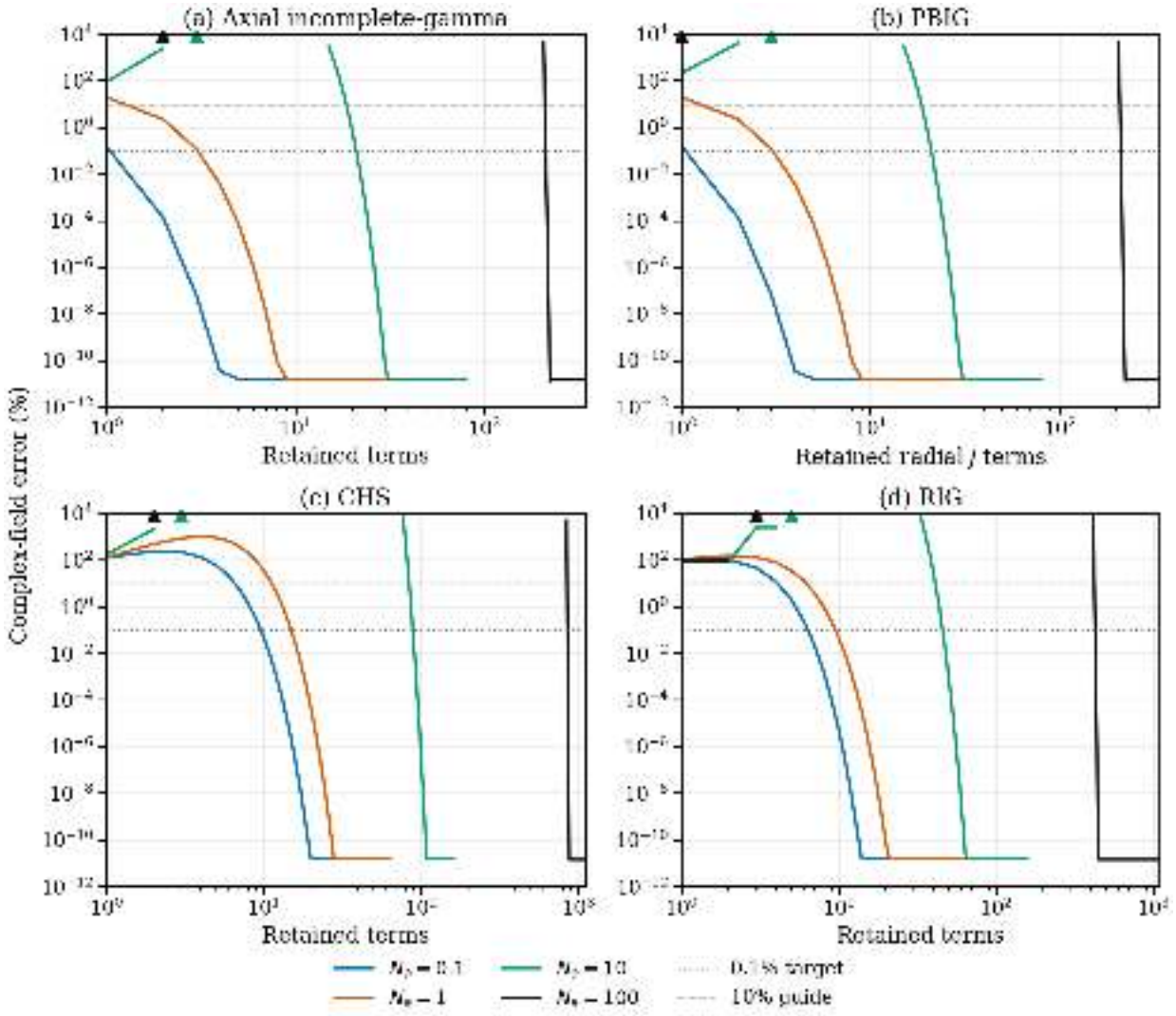


Figure 7: Sampled complex-field convergence for $\tau = 1$ and $N_a = 0.1, 1, 10, 100$: (a) axial incomplete-gamma series on the five-point axis stencil; (b) PBIG, (c) CHS and (d) RIG on the identical 15-point xz stencil, $0.5 \leq z/f \leq 1.5$. The ordinate is $100\epsilon_n$ from Eq. 172. The dotted and dashed lines mark 0.1% and 10%, respectively; upward triangles indicate errors above the displayed 10^4% ceiling. Complete unbounded error traces are retained in the numerical data. Orders and working precision are specified in the text and SI.

distinguishes the search for qualified settings from a fresh evaluation at those settings. These pointwise examples complement the common-stencil comparison; their different samples and timing conventions are reported separately. SI Section 10.3.1 gives the samples, errors, orders, timing conventions and cancellation checks.

6 Physical results and practical relations

6.1 Finite-Fresnel focal structure

Figure 8 evaluates Eq. 100 for circular top-hat illumination over $N_a = 0.1, 1, 10, 30, 100$, and 1000. The xz rows set $\tilde{y} = 0$ and vary $\tilde{x}$; the yz rows set $\tilde{x} = 0$ and vary $\tilde{y}$, with $\tilde{y} = N_a y/a$. Every axial panel uses $\tilde{z} = z/f$. High-N_a panels resolve a narrower range around the dashed nominal plane at 1. The yz maps describe intensity and axial extent along sheet height; focused-x thickness is separately obtained from transverse half-maximum roots.

6.2 Practical FWHM formulas and applicability

The complete field, limiting formulas and moment expressions provide complementary routes to a light-sheet width. A declared measurement plane and a qualified connected lobe precede formula selection. At nominal focus, the top-hat and Gaussian limits give elementary estimates; the moment formulas retain the Gaussian truncation continuously. For the rectangle, their coefficients are direct incomplete-gamma expressions. For the circle, one chord quadrature or converged CHS coefficients retain the finite boundary and non-focused phase. The compact axial moment expressions use real strip moments and require no pupil quadrature, while their strong-focus reduction has its own complete-field error.

For nominal transverse thickness, continuous moments give maximum sampled errors below 0.5% for both pupils over the stated tested domains. The axial choice also depends on the width of the focal lobe and variation of the non-focused field. The three-region rule and the derived and calibrated axial expressions are compared against qualified complete-field widths in SI Section 12.2 and SI Section 12.3. The formula guide in SI Section 12.6 lists each geometry's equations, evaluation route, accuracy evidence and numerical fallback. Additional fitted and tabulated alternatives and comparisons on common reference points are provided in SI Section 12.5.

Outside the near-nominal regime, the same complete field determines the displaced peak and the transverse width at that plane. Plane-dependent moments can approximate this width after z_p has been identified; their local accuracy is assessed separately from nominal-focus accuracy. The minimum-thickness plane z_t is a different stationary point. A minimum estimate is useful for sheet design, but it does not by itself locate the axial intensity peak or its two half-height crossings.

The circular top-hat transition and its endpoint-based estimate are given with their derivation in Section 3.5 and Figure 5. Complete slice roots retain the intermediate Fresnel-number dependence, while the circular moment coefficients supply a compact nominal-plane approximation.

6.3 Circular versus rectangular pupils

The rectangular pupil defines a distinct illumination geometry and an exact separable benchmark. At large Fresnel number, the central portion of a circular pupil approaches a fixed-width strip and its focused-x-axis profile tends toward the rectangular sinc result. At $N_a \sim 1$, the complete circular boundary contributes coherently and the two profiles differ.

A comparison is meaningful only after the matching condition is stated. Equal maximum width fixes the same marginal ray angle; equal area, transmitted power, second moment, and effective numerical aperture impose different constraints and generally give different profiles. SI Section 13 reports all of these conventions and the corresponding exact curves. No geometry is described as universally superior.

6.4 Representative dimensional application

Table 1 uses $\lambda = 633$ nm in air and $f = 400$ mm. The aperture diameter is chosen from the requested N_a, so the table compares Fresnel regimes rather than holding diameter fixed. Low-Fresnel cases exhibit displacement, oscillations or sensitivity of the broad-peak estimate; the table retains each independently qualified metric. At $N_a = 100$ the nominal and peak planes nearly coincide.

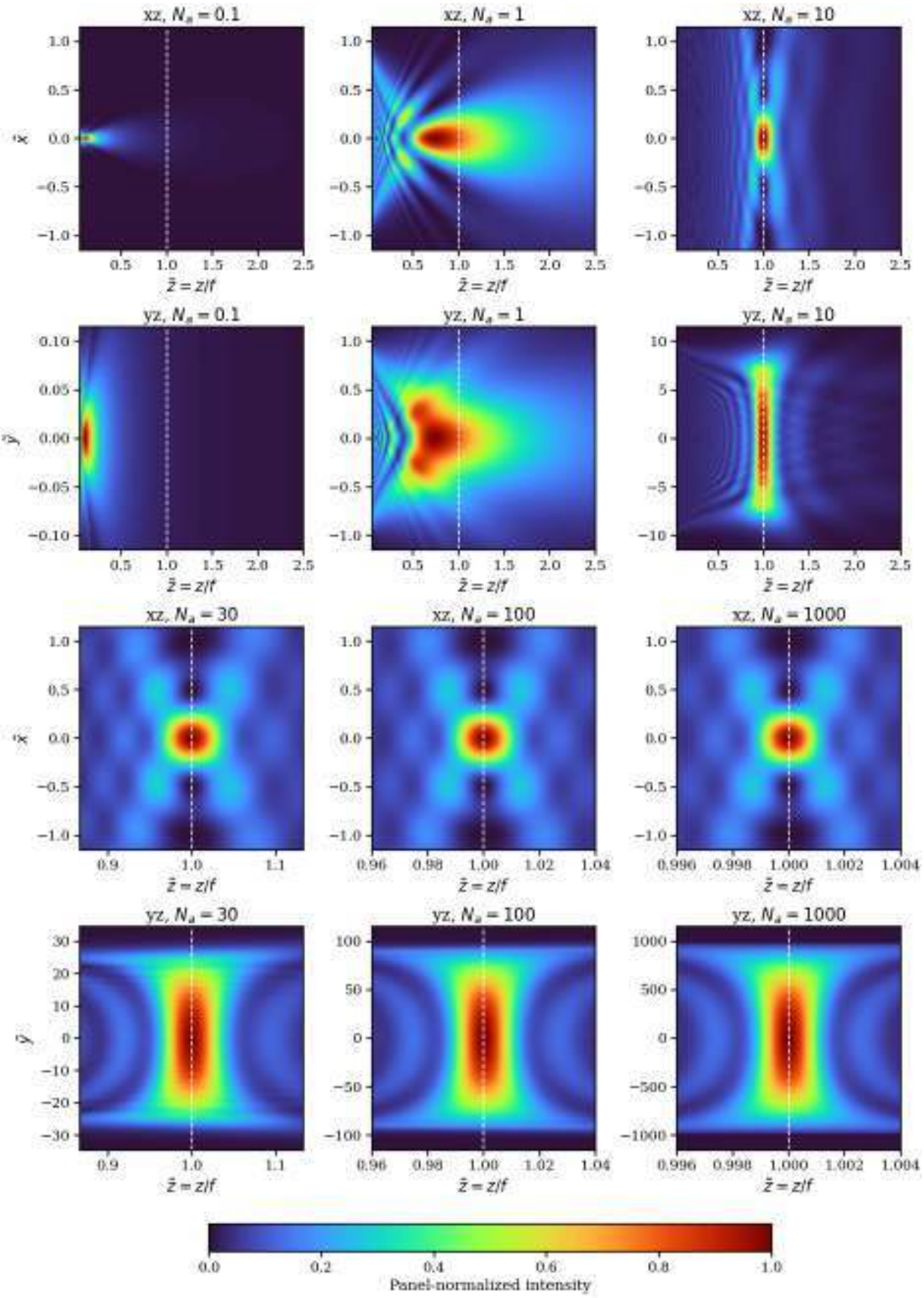


Figure 8: Circular top-hat propagation matrix. Rows 1–2 show xz and yz planes at $N_a = 0.1, 1, 10$; rows 3–4 show the same planes at $N_a = 30, 100, 1000$. Scalar maps use the Turbo colormap and are normalized panel by panel.

Table 1: Complete circular-field examples with qualified broad-profile metrics for $\lambda = 633$ nm and $f = 400$ mm. The pupil diameter is $D_a = 2a = 2\sqrt{N_a \lambda f}$. In the three rows containing unresolved entries, the broad-peak position and axial width are sensitive to regression settings; the peak-plane transverse width is consequently withheld, while the independently qualified nominal-plane width remains available. All Gaussian rows use $\tau = 1$, for which the Gaussian $1/e^2$ intensity diameter equals D_a.

Illumination	N_a	D_a (mm)	z_p (mm)	$\mathrm{FWHM}_{x,p}$ (μm)	$\mathrm{FWHM}_{x,f}$ (μm)	FWHM_z (mm)
top-hat	0.1	0.318	38.83	79.80	818.28	51.16
Gaussian, $\tau = 1$	0.1	0.318	unresolved	unresolved	899.84	unresolved
top-hat	1	1.006	unresolved	unresolved	244.16	unresolved
Gaussian, $\tau = 1$	1	1.006	unresolved	unresolved	271.85	unresolved
top-hat	10	3.182	396.86	69.34	69.87	71.15
Gaussian, $\tau = 1$	10	3.182	396.55	80.52	81.13	82.77
top-hat	100	10.064	399.97	22.27	22.27	6.99
Gaussian, $\tau = 1$	100	10.064	399.97	25.75	25.76	8.18

The complete $f = 100$ and 400 mm, $\tau = 0, 1, 2$, and $N_a = 0.1, 1, 10, 100$ table is in SI Section 13. Each metric is reported independently. For weakly truncated low-Fresnel cases, an unbracketed axial half crossing is marked unresolved in the stated search window, while the established transverse widths remain available.

For plane-parallel air–glass–sample propagation at low numerical aperture, the paraxial focus is governed by the reduced optical distance $\sum_j d_j/n_j$. In the example with 370 mm of air, 1 mm of glass ($n = 1.52$), water ($n = 1.333$), and $f = 400$ mm, the nominal unrefracted sample depth is 29.000 mm and the refracted paraxial depth is 39.113 mm. Exact Snell tracing through 5-mm ray height differs from the latter by at most 1.375 μm. For a fixed incident ray bundle, Snell's law conserves $n \sin(\theta)$ and hence numerical aperture across the parallel interfaces. The leading transverse scale λ_0/NA is then unchanged, whereas the physical axial scale $n\lambda_0/\mathrm{NA}^2$ increases with the sample index. SI Section 14 gives the reduced-distance and full-Snell derivations and the assumptions of this low-NA comparison.

7 Discussion

The central analytical result is the elimination of the focused pupil coordinate from the physical anisotropic Fresnel kernel while retaining the finite circular boundary, Gaussian truncation, arbitrary observation coordinates, and physical propagation prefactor. This produces a stable one-quadrature point evaluator. The rectangular family follows from the same kernel and supplies an exact separable benchmark.

The formulation complements established methods. The invariant-axis rectangular result is the closest cylindrical baseline [6]. ENZ is broader for arbitrary circular-pupil aberrations and vector extensions [16, 17], whereas the present slice form keeps aperture radius, beam radius, focal length, propagation distance, and observation point explicit without an intervening pupil expansion. The quadratic/elliptical corollary widens the useful class but does not cover arbitrary non-Gaussian two-dimensional amplitudes or higher-order phase functions analytically.

The results also separate several quantities that are sometimes conflated. $\mathrm{FWHM}_{x,f}$ describes the nominal focal plane, $\mathrm{FWHM}_{x,p}$ the principal intensity-peak plane, and FWHM_z the connected axial intensity width. At low Fresnel number, the two transverse planes can differ strongly and a two-sided FWHM_z may remain unbracketed or sensitive to broad-lobe identification. Full field profiles then describe the illumination geometry; a qualified downstream half-width can supply an equivalent extent when the upstream crossing is unavailable.

Maximum-error-first selection distinguishes the accuracy of limiting formulas, continuous moment expressions and complete-field width calculations. The SI compares additional empirical approximations on common qualified reference points. These practical width-formula comparisons use the stated broad-profile convention, with numerical and regression sensitivity recorded independently; the matched raw-field root checks in Section 5 separately test agreement between field representations. Complete fields remain available for shifted,

oscillatory or otherwise unqualified cases. The analytical series provide insight and independent validation; their stable finite-order evaluation becomes increasingly demanding as cancellation grows.

The main limitations are the scalar, homogeneous, paraxial, ideal-lens assumptions. Misalignment, measured wavefront error, scattering specimens, and high numerical aperture require extensions. A low-NA plane-parallel air–glass–sample example is retained in SI Section 14 only as an illustrative reduced-distance calculation; it is not evidence that scalar propagation captures high-NA interface aberrations [25].

8 Conclusion

One scalar paraxial Fresnel formulation now covers the declared circular/rectangular and Gaussian/top-hat cylindrical-lens families. The circular hard stop is retained exactly through an analytical focused-coordinate strip and one remaining quadrature, while rectangular pupils separate into the same strip function. Special fields, independently verified analytical series, and explicit local and axial metrics connect the field theory to light-sheet design.

The resulting calculations quantify finite-Fresnel focal displacement, nominal- versus peak-plane thickness, and axial extent. The moment-based transverse formula gives a simple semianalytical description across truncation, with maximum sampled errors below 0.5% for both pupil geometries. Connected exact-field roots, strong-focus limits, and derived and calibrated moment expressions provide complementary axial-width representations. Together these results connect the common diffraction theory to practical cylindrical-light-sheet dimensions while retaining the physical pupil, beam, wavelength, and focal length.

Availability of data and code

The analytical derivations, numerical methods and reported validation results are presented in the manuscript and Supporting Information. The code and data supporting this study are available from the corresponding authors on reasonable request. The exact slice and separable fields are the scientific reference; compact and tabulated laws are bounded accelerators within their declared domains.

Author contributions

S.Y. conceived the problem, defined the light-sheet application, developed the theoretical scope, and drafted the manuscript. S.Y. and D.P. discussed the optical model and interpretation. The analytical and numerical framework was developed and validated for the present work. Both authors reviewed the manuscript.

Paper drafting and writing, derivations, code development, numerical analysis, figure generation and data processing were assisted by OpenAI GPT-5.6-Sol and GPT-6-Astra large language models, using `thinking_effort` settings of `xhigh` or `max`. The computational workflow used Python, with SymPy for symbolic verification, NumPy and SciPy for numerical algorithms and data processing, mpmath for high-precision special-function checks, and Matplotlib for plotting.

Competing interests

The authors declare no competing interests.

Acknowledgements

The theoretical problem arose from the development of a modular light-sheet optical microscopy platform at the Institute of Information and Communication Technologies – Bulgarian Academy of Sciences. The authors acknowledge the broader VIBraTE research context supported by the European Union ERA Chair programme (project 101086815).

References

[1] Jan Huisken, Jim Swoger, Filippo Del Bene, Joachim Wittbrodt, and Ernst H. K. Stelzer. Optical sectioning deep inside live embryos by selective plane illumination microscopy. *Science*, 305(5686):1007–1009, 2004. https://doi.org/10.1126/science.1100035.

[2] Ernst H. K. Stelzer. Light-sheet fluorescence microscopy for quantitative biology. *Nature Methods*, 12: 23–26, 2015. https://doi.org/10.1038/nmeth.3219.

[3] Rory M. Power and Jan Huisken. A guide to light-sheet fluorescence microscopy for multiscale imaging. *Nature Methods*, 14:360–373, 2017. https://doi.org/10.1038/nmeth.4224.

[4] H. Kogelnik and T. Li. Laser beams and resonators. *Proceedings of the IEEE*, 54(10):1312–1329, 1966. https://doi.org/10.1109/PROC.1966.5119.

[5] Adam K. Glaser, Ye Chen, Chengbo Yin, Linpeng Wei, Lindsey A. Barner, Nicholas P. Reder, and Jonathan T. C. Liu. Multidirectional digital scanned light-sheet microscopy enables uniform fluorescence excitation and contrast-enhanced imaging. *Scientific Reports*, 8:13878, 2018. https://doi.org/10.1038/s41598-018-32367-5.

[6] Colin J. R. Sheppard. Cylindrical lenses—focusing and imaging: A review. *Applied Optics*, 52(4):538–545, 2013. https://doi.org/10.1364/AO.52.000538.

[7] C. W. McCutchen. Generalized aperture and the three-dimensional diffraction image. *Journal of the Optical Society of America*, 54:240–244, 1964. https://doi.org/10.1364/JOSA.54.000240.

[8] Colin J. R. Sheppard. Diffraction of a focused wave by an aperture: A new perspective. *Journal of the Optical Society of America A*, 32(4):623–629, 2015. https://doi.org/10.1364/JOSAA.32.000623.

[9] Yajun Li and Emil Wolf. Three-dimensional intensity distribution near the focus in systems of different fresnel numbers. *Journal of the Optical Society of America A*, 1(8):801–808, 1984. https://doi.org/10.1364/JOSAA.1.000801.

[10] C. J. R. Sheppard. Imaging in optical systems of finite fresnel number. *Journal of the Optical Society of America A*, 3(9):1428–1432, 1986. https://doi.org/10.1364/JOSAA.3.001428.

[11] Virendra N. Mahajan. Uniform versus gaussian beams: A comparison of the effects of diffraction, obscuration, and aberrations. *Journal of the Optical Society of America A*, 3(4):470–485, 1986. https://doi.org/10.1364/JOSAA.3.000470.

[12] Virendra N. Mahajan. Axial irradiance of a focused beam. *Journal of the Optical Society of America A*, 22(9):1814–1823, 2005. https://doi.org/10.1364/JOSAA.22.001814.

[13] Yajun Li and F. T. S. Yu. Intensity distribution near the focus of an apertured focused gaussian beam. *Optics Communications*, 70(1):1–7, 1989. https://doi.org/10.1016/0030-4018(89)90197-1.

[14] Hakan Urey. Spot size, depth-of-focus, and diffraction ring intensity formulas for truncated gaussian beams. *Applied Optics*, 43(3):620–625, 2004. https://doi.org/10.1364/AO.43.000620.

[15] K. Dupraz, A. Martens, J. M. Rax, and F. Zomer. Diffraction of gaussian and laguerre–gauss beams from a circular aperture using the moment expansion method. *Journal of the Optical Society of America A*, 40(1):27–34, 2023. https://doi.org/10.1364/JOSAA.470148.

[16] Augustus J. E. M. Janssen. Extended nijboer–zernike approach for the computation of optical point-spread functions. *Journal of the Optical Society of America A*, 19(5):849–857, 2002. https://doi.org/10.1364/JOSAA.19.000849.

[17] Joseph J. M. Braat, Peter Dirksen, Augustus J. E. M. Janssen, and Arthur S. van de Nes. Extended nijboer–zernike representation of the vector field in the focal region of an aberrated high-aperture optical system. *Journal of the Optical Society of America A*, 20(12):2281–2292, 2003. https://doi.org/10.1364/JOSAA.20.002281.

[18] Subhajit B. Purnapatra and Partha P. Mondal. Determination of electric field at and near the focus of a cylindrical lens for applications in fluorescence microscopy. *AIP Advances*, 3:052124, 2013. https://doi.org/10.1063/1.4807670.

[19] Glen D. Gillen, Kendra Baughman, and Shekhar Guha. Application of hertz vector diffraction theory to the diffraction of focused gaussian beams and calculations of focal parameters. *Optics Express*, 17(3): 1478–1492, 2009. https://doi.org/10.1364/OE.17.001478.

[20] Joseph W. Goodman. *Introduction to Fourier Optics*. W. H. Freeman, 4 edition, 2017.

[21] Max Born and Emil Wolf. *Principles of Optics*. Cambridge University Press, 7 edition, 1999.

[22] National Institute of Standards and Technology. NIST Digital Library of Mathematical Functions: Confluent hypergeometric functions. URL https://dlmf.nist.gov/13. Chapter 13, Sections 13.2 and 13.4, Eqs. 13.2.4 and 13.4.1. Accessed 8 October 2026.

[23] Charles R. Harris et al. Array programming with numpy. *Nature*, 585:357–362, 2020. https://doi.org/10.1038/s41586-020-2649-2.

[24] Pauli Virtanen et al. Scipy 1.0: Fundamental algorithms for scientific computing in python. *Nature Methods*, 17:261–272, 2020. https://doi.org/10.1038/s41592-019-0686-2.

[25] Peter Török. Focusing of electromagnetic waves through a dielectric interface by lenses of finite fresnel number. *Journal of the Optical Society of America A*, 15(12):3009–3015, 1998. https://doi.org/10.1364/JOSAA.15.003009.